



Cepheids in M31: The PAndromeda Cepheid Sample

Mihael Kodric^{1,2}, Arno Riffesser^{1,2}, Ulrich Hopp^{1,2}, Claus Goessl^{1,2}, Stella Seitz^{1,2} , Ralf Bender^{1,2} , Johannes Koppenhoefer^{1,2}, Christian Obermeier^{1,2} , Jan Snigula^{1,2}, Chien-Hsiu Lee^{1,5}, W. S. Burgett³ , P. W. Draper⁴ , K. W. Hodapp³ , N. Kaiser³ ,

R.-P. Kudritzki³, N. Metcalfe^{4,5} , J. L. Tonry³ , and R. J. Wainscoat³ 

¹University Observatory Munich, Scheinerstrasse 1, D-81679 Munich, Germany; kodric@usm.lmu.de

²Max Planck Institute for Extraterrestrial Physics, Giessenbachstrasse, D-85748 Garching, Germany

³Institute for Astronomy, University of Hawaii at Manoa, Honolulu, HI 96822, USA

⁴Department of Physics, Durham University, South Road, Durham DH1 3LE, UK

⁵Subaru Telescope, NAOJ, 650 N. Aohoku Pl., Hilo, HI 96720, USA

Received 2018 May 14; revised 2018 June 15; accepted 2018 June 19; published 2018 August 29

Abstract

We present the largest Cepheid sample in M31 based on the complete Pan-STARRS1 survey of Andromeda (PAndromeda) in the r_{P1} , i_{P1} , and g_{P1} bands. We find 2686 Cepheids with 1662 fundamental-mode Cepheids, 307 first-overtone Cepheids, 278 type II Cepheids, and 439 Cepheids with undetermined Cepheid type. Using the method developed by Kodric et al., we identify Cepheids by using a three-dimensional parameter space of Fourier parameters of the Cepheid light curves combined with a color cut and other selection criteria. This is an unbiased approach to identify Cepheids and results in a homogeneous Cepheid sample. The period–luminosity relations obtained for our sample have smaller dispersions than in our previous work. We find a broken slope that we previously observed with *HST* data in Kodric et al., albeit with a lower significance.

Key words: catalogs – distance scale – galaxies: individual (M31) – Local Group – stars: variables: Cepheids

Supporting material: machine-readable tables, tar.gz file

1. Introduction

Cepheids are standard candles, and their period–luminosity relation (PLR), sometimes referred to as the Leavitt law (Leavitt 1908; Leavitt & Pickering 1912), can be used to determine extragalactic distances. In order to be used for distance determination, the PLR needs to be calibrated by using Cepheids with already known distances. There are multiple galaxies (so-called anchor galaxies) with well-known distances that host the Cepheids used for this calibration. Typically, one or a combination of these anchor galaxies are used for the calibration: the Milky Way, the Magellanic Clouds, M106, and the Andromeda galaxy (M31). Cepheids in the Milky Way need very precise parallaxes. Until recently, the number of Cepheids with accurate enough parallaxes was very limited. The *Gaia* mission (Gaia Collaboration et al. 2016) remedied this problem and will keep improving the parallaxes and therefore the precision of the calibration (see Riess et al. 2018 for an application of the *Gaia* DR2 parallaxes to Milky Way Cepheids). The Magellanic Clouds have been studied extensively (see, e.g., Soszyński et al. 2015 and Udalski et al. 2015 for the OGLE survey and Gieren et al. 2015 for the Araucaria project), and there are a lot of known Cepheids. Pietrzyński et al. (2013) used eclipsing binaries to determine the distance to the Large Magellanic Cloud (LMC) with an uncertainty of only 2%. For M106, a very accurate distance has been determined geometrically by a maser (Humphreys et al. 2013), and it is therefore also used as an anchor galaxy (Hoffmann & Macri 2015). Galaxy M31 is relatively nearby, the disk has a solar metallicity, and the full range of the PLR can be observed from ground- and space-based observatories in the optical and near-infrared. These advantages are partly compromised by the large extent on the sky, and significant crowding caused by the large inclination are major issues for an M31 Cepheid survey. There have, however, been multiple surveys of M31 Cepheids,

and hence there are multiple Cepheid samples: the PAndromeda Cepheid sample (Kodric et al. 2013; hereafter K13) with 2009 Cepheids, the Vilardell et al. (2006) sample with 416 Cepheids, the 332 Cepheid sample from the DIRECT survey (Kaluzny et al. 1998, 1999; Stanek et al. 1998, 1999; Mochejska et al. 1999; Bonanos et al. 2003), and the WECAPP sample (Fliri et al. 2006) with 126 Cepheids. There are also Cepheid samples making use of the PHAT *HST* survey of M31 (Dalcanton et al. 2012): the Riess et al. (2012) sample with 68 Cepheids, the Kodric et al. (2015; hereafter K15) sample with 371 Cepheids, and the Wagner-Kaiser et al. (2015) sample with 175 Cepheids. See also Lee (2017) for a summary of time-domain studies in M31.

The PLR calibration is not the only goal of the PAndromeda project; it is also intended to study systematic effects on the PLR. The effect of metallicity on the PLR needs further investigation (see, e.g., Freedman & Madore 2011; Majaess et al. 2011). A metallicity effect on the PLR has to be accounted for when using the low-metallicity Magellanic Cloud PLR to determine the distance to a galaxy with a Milky Way–like metallicity like the Andromeda galaxy (M31). Another issue with the PLR is the possible existence of a broken slope (Sandage et al. 2009). The existence of a broken slope is heavily discussed in the literature. Ngeow et al. (2008) found a broken slope but linear relations in the K_s band and the Wesenheit PLR. Inno et al. (2013), however, found linear Wesenheit PLRs, while García-Varela et al. (2013) found no linear relations but rather exponential ones. In K15, we found a significant broken slope in all relations, including the Wesenheit PLR. The Cepheid sample we obtain here is used in Kodric et al. (2018; hereafter K18b), where we combine it with the PHAT data to obtain the largest *HST* Cepheid sample for M31 and investigate the broken slope. Since Cepheids are part of the distance ladder used to determine the Hubble constant (H_0), the study of these systematic effects is not only

important for the value and error budget of H_0 but also for ascertaining how universal the PLR is in different galaxies. Riess et al. (2016) used Cepheids as part of their distance ladder in order to determine H_0 with an uncertainty level of only 2.4%. Freedman & Madore (2010) summarized previous projects focused on determining H_0 (for a more recent summary, see Riess et al. 2016 and references therein). Another uncertainty in the determination of H_0 is the handling of outliers in the PLR, which is still discussed in the literature (e.g., Efstathiou 2014; Becker et al. 2015).

This paper is structured as follows. In Section 2, we discuss the PAndromeda survey and the data reduction procedure used for this paper, which is different from that of K13. In Section 3, we describe the Cepheid detection and classification. Section 4 describes the PAndromeda Cepheid catalog. The results are discussed in Section 5, followed by the conclusion in Section 6.

2. PAndromeda Data

PAndromeda is a Pan-STARRS1 (PS1; Kaiser et al. 2002; Hodapp et al. 2004; Tonry & Onaka 2009; Tonry et al. 2012; Chambers et al. 2016) survey dedicated to monitoring the Andromeda galaxy (M31). The original goal of the survey was microlensing (Lee et al. 2012), but the focus has shifted toward Cepheids (K13; Lee et al. 2013; K15), eclipsing binaries (Lee et al. 2014a), and luminous blue variables (Lee et al. 2014b). The 1.8 m PS1 telescope has a very large field of view (FOV) with $\sim 7 \text{ deg}^2$, which makes it ideal for observing M31, since the complete disk can be observed in one exposure.

2.1. PAndromeda Survey

The galaxy M31 was observed from 2009 August 31 to 2010 January 21, 2010 July 23 to 2010 December 27, 2011 July 25 to 2011 November 22, and 2012 July 28 to 2012 October 31, with usually two visits per night in the g_{P1} , r_{P1} , and i_{P1} bands (see Tonry et al. 2012 for information on the PS1 filter system). The general exposure time is 60 s per frame, and each epoch (visit) is a stack of typically seven frames in the r_{P1} band and five frames in the g_{P1} and i_{P1} bands. The creation of this visit stack is described in the next section. Figure 1 shows the distribution of the number of frames making up one epoch. In total, there are 420 epochs in the r_{P1} band, 262 epochs in the i_{P1} band, and 56 epochs in the g_{P1} band. Due to masking (which will be discussed in the following section), the light curves usually have less epochs, so this is the maximum number of epochs. In addition, we disregard epochs that are based on less than three frames. In total, PAndromeda has taken 2511 frames in the r_{P1} band with a combined exposure time of 157,904 s ($\approx 43.86 \text{ hr}$), 1260 frames in the i_{P1} band with a total of 75,840 s ($\approx 21.07 \text{ hr}$), and 246 frames in the g_{P1} band with a combined exposure time of 15,048 s ($\approx 4.18 \text{ hr}$).

The gigapixel camera (GPC) consists of 60 orthogonal transfer arrays (OTAs), where each OTA is made up of an array of 8×8 cells. One OTA has an FOV of $21' \times 21'$. The pixel scale is $0''.25 \text{ pixel}^{-1}$. The PS1 image-processing pipeline (IPP; Magnier 2006) provides us with astrometrically aligned frames (the frames are also bias- and flat-field-corrected). During the alignment, the exposures are remapped to a common grid, the so-called skycells. Only the first data reduction steps are done by the IPP; the other steps, done by ourselves, are discussed in the next section. Compared to K13, we changed the layout and size of the skycells so that they now cover $6647 \text{ pixels} \times 6647 \text{ pixels}$

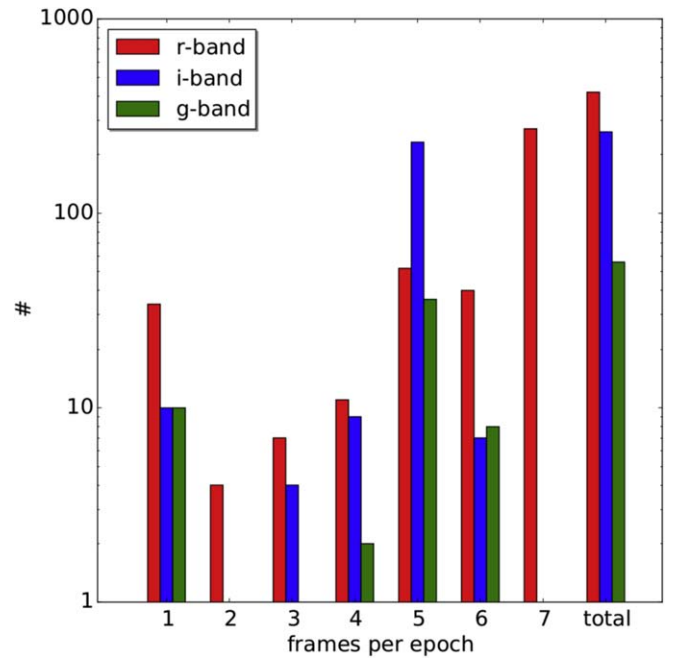


Figure 1. Number of frames contributing to each epoch. For Cepheid light curves, we require at least three frames per epoch. In total, the PAndromeda data consist of up to 420 epochs in the r_{P1} band, up to 262 epochs in the i_{P1} band, and up to 56 epochs in the g_{P1} band.

(i.e., 27.7×27.7) and use the intrinsic pixel scale of $0''.25$. Also, we defined the skycells such that they overlap (by $6'$), in order to have a simple way to check our data reduction for consistency. The covered area is $\sim 7 \text{ deg}^2$ in the r_{P1} and i_{P1} bands and $\sim 6.8 \text{ deg}^2$ in the g_{P1} band. The central six skycells were split during our data reduction into four smaller skycells with $3524 \text{ pixels} \times 3524 \text{ pixels}$ (i.e., 14.7×14.7), for reasons discussed in the next section. The area covered in the g_{P1} band is smaller, since skycells 003, 004, 005, 006, 012, and 028 are not used due to the lack of data in their skycells. The area in K13 (with $\sim 2.6 \text{ deg}^2$) is much smaller than the area analyzed here. The skycell layout for this work (hereafter K18a), as well as for K13, is shown in the Appendix.

2.2. PAndromeda Data Reduction

The data reduction is based on our previous pipeline used in K13. The overall approach of using difference imaging (Alard & Lupton 1998) is the same. Apart from changing certain details, the biggest change is to mask a large fraction of the images in order to minimize systematic errors that are due to the poor PS1 image quality. The trade-off for less systematics is a larger statistical error caused by the rigorous masking. This was mainly done to help with the microlensing search (Lee et al. 2012), which was originally the main scientific goal of PAndromeda. As far as Cepheid light curves are concerned, the fact of having more statistical noise is usually negated by the large increase in epochs. But some area is lost or has substantially less epochs due to the masking. Therefore, we do not recover all Cepheids found in K13 and all eclipsing binaries found in Lee et al. (2014a).

As mentioned in the previous section, our data reduction starts with astrometrically aligned frames provided by the IPP (Magnier 2006) that are already debiased and flat-field-corrected. Our pipeline (see also Lee et al. 2012; Koppenhoefer et al. 2013; K13) uses the AstroWISE data-management

environment (Valentijn et al. 2007). In the first step, where we ingest the frames provided by IPP into the AstroWISE database, we apply multiple masks. We use most of the masking flags already provided by IPP. The quality of these original masks was not sufficient, so we improved those masks and provided them to the IPP in order to reprocess all of our raw data using these new mask files. This step was necessary since the masks are based on the defects on the OTA cell level, and applying the masks before the skycell regridding is computationally more efficient. We also use the ghost masks provided by IPP but significantly increase the masking, since the position of the ghost model is sometimes off. We also mask satellite tracks using the linear Hough transform algorithm that is implemented in AstroWISE, and we use manually created masks that we have for a few hundred frames. Saturated pixels are also masked. Since there are offsets between the OTAs, we only use the dominant OTA in each skycell and mask the other OTAs. This implies that we mask up to 75% for the rare case where four OTAs are in one frame with the same area. This OTA masking is quite extreme, but it ensures that there are no systematic jumps inside a frame and that we can photometrically align the frames to each other. After applying these masks, we only use those frames that have more than 20% unmasked pixels in the central region of the frame (pixels 1661–4985 in x and y). The mean masking over all frames in all skycells is 64% in the r_{P1} and i_{P1} bands and 65% in the g_{P1} band. The mean masking per skycell ranges from 48% to 83% in the r_{P1} band, 48% to 82% in the i_{P1} band, and 43% to 85% in the g_{P1} band.

As can be seen in Figures 27–29, the central six skycells are each divided into four smaller skycells. The point-spread function (PSF) varies slightly over the FOV of the GPC. The PSF is broadest on the edges of the GPC but also blurred in the center of the GPC. Over the PAndromeda observing campaign, the center of the GPC was pointed on different skycells. Due to this, the central six skycells showed the largest PSF variation. By splitting them into smaller frames, the variation inside these new skycells is significantly reduced. This ensures that our PSF photometry, which uses a constant PSF model for a skycell, performs well.

In order to perform difference imaging, we need to construct so-called reference frames. A reference frame is a stack of the images with the best PSF. The frames are photometrically aligned so that the sky background and zero point are the same. Masked areas in one frame (if the masked region is not too large) are replaced from another frame with an almost similar PSF. The frames are assigned weights according to the inverse of the squared product of the seeing and the mean error. The reference frame is the weighted stack of these frames. In the r_{P1} and i_{P1} bands, we use 100 frames for the reference frame. For the g_{P1} band, we use 40 frames. Additionally, we require the original position angle to be zero or a multiple of 90° in the r_{P1} and i_{P1} bands. The reason for this is that we want to limit the increased noise caused by, e.g., chip gaps or bleeding to the four cardinal directions. The observing strategy required the second visit in one night to have a position angle of 90° . Unfortunately, there were also a significant number of frames taken with a random position angle. We disregard those for the reference frame in the r_{P1} and i_{P1} bands but have to use them in the g_{P1} band, because in this band we do not have enough data. In K13, we used the 70 best-seeing frames, but here we also selected according to masking. Since we increased the masking

drastically, we have to make sure that the reference frames cover as much area as possible. Everything that is masked in the reference frame will be lost, even if there are frames that have data in these masked regions. Due to the fact that the masking fraction and the seeing are not correlated, we first select seven times more frames for the reference frame where the masking is the lowest and then select the best-seeing frames from those frames. The frame that is used to photometrically align the other frames is one of the 10 best-seeing frames that overlaps the most with the other frames. The reason for this is that the alignment works better the more area the frames have in common. Since we wanted to limit the area lost due to the new strict masking, we also require that a frame does not increase the masking in the reference frame too much. Pixels that are masked in all but one frame will still be dominant in the reference frame. During the creation of the reference frame, each frame contributing to it is checked if including it in the stack would decrease the unmasked area in the reference frame by more than 1%. If that is the case, the frame will be dropped from the reference frame. Therefore, the final reference frame can include less than 100 (r_{P1} and i_{P1} bands) or 40 (g_{P1} band) frames, respectively. Each reference frame is calculated twice. The first time, the sources are detected using SExtractor (Bertin & Arnouts 1996). The reference frame is inspected, and if there are, e.g., satellite tracks missed by the algorithm or ghosts, etc., we create manual masks for the input frames. This first reference frame is then used to photometrically align the input frames for the creation of the final second reference frame. In the second run, we use DAOPHOT (Stetson 1987) to detect the sources. Due to the crowding in M31, SExtractor sometimes determines a wrong position of a star, while DAOPHOT is optimized for high crowding. We perform PSF photometry on the positions identified with DAOPHOT on a background-subtracted reference frame. The neighboring stars are iteratively subtracted in order to account for the crowding. As in K13, we fit a bicubic spline model to determine the background (sky and M31). For each skycell, we determine a PSF model but do not vary it over the reference frame. The flux calibration is done as in K13; however, we do not use the Sloan Digital Sky Survey (SDSS; Abazajian et al. 2009) for the calibration but rather the PS1 PV2 catalog (Chambers et al. 2016). The reason for this is that the SDSS catalog is very sparsely populated in the central region of M31. With the PV2 catalog, we have a lot of comparison stars, so that we are able to also correct for PSF variation over the field by modeling the zero point with a spline.

For the difference imaging, we also need to create so-called visit stacks, which are stacks of all frames from one visit. Ideally, there should have been two visits of M31 per night, one in the first half of the night and one in the second half. The data taken have significant deviations from that. Sometimes the second visit was done right after the first, or there were three visits or visits with less frames. Also, the total integration time per visit changed several times in order to balance the total exposure time between the r_{P1} and i_{P1} bands. So, instead of automatically splitting the data of one night into two visit stacks, we grouped all the frames by hand into visit stacks with a stack depth as homogeneous as possible. The frames of a visit stack are photometrically aligned such that the sky background and zero point are the same. The weighted stack of these frames is photometrically aligned to the reference frame such that the visit stack and reference frame have the same zero point and

sky background. Note that the visit stack has a smaller signal-to-noise ratio, since the reference frame is much deeper and the PSF is different, i.e., usually worse. As described in K13, the PSF of the reference frame is aligned to the visit stack by determining a convolution kernel when calculating the difference frame. Compared to K13, we decreased the size of the area one convolution kernel uses in order to better account for differences not only in PSF size but also PSF shape. We also masked out all sources brighter than 18 mag in the r_{P1} band, since those bright sources are not relevant for our science cases and are producing residuals in the difference frame. The PSF photometry on the difference frame uses the PSF constructed from the convolved reference frame.

In order to obtain the flux in one epoch of the light curve of a resolved source, the flux in the difference frame is added to the flux in the reference frame. Since the skycells overlap, the light curve can be constructed as a combination of measurements from different skycells. For the case where a resolved source has measurements of one epoch in multiple skycells, we use the measurement with the smallest error. For our Cepheid detection, we only use epochs in the light curve that have a signal-to-noise ratio larger than two and where the visit stack has more than two frames (the published light curves include those epochs for consistency). In total, we have detected 7,226,125 unique sources, where 3,348,137 unique sources have data in at least the r_{P1} band. For all sources that have r_{P1} -band data, we determine the periodicity of the light curve with SigSpec (Reegen 2007). In K13, we explained in detail how we determined the periods and period errors. We have not changed any parameter of the period determination, since the procedure described in K13 works very well. For the period error determination, we increased the number of bootstrapping samples from 1000 in K13 to 10,000. The error rescaling factor described in K13 that was necessary due to the change of the pixel scale is as expected, 1.0, and therefore not necessary anymore. We use the AB magnitude system throughout this paper and in the published data.

3. Cepheid Detection and Classification

The goal is to find as many Cepheids as possible in an unbiased way. We could look through all periodic light curves by eye and select those that have a typical shape for a Cepheid. The problem with this approach is that different pulsators are sometimes hard to distinguish, especially in a noisy light curve. Also, the selection would be unreproducible and not objective. Therefore, we use essentially the same procedure we developed in K13 in order to be as unbiased as possible. We apply some selection criteria and manually determine a Cepheid sample from high signal-to-noise light curves and use the Fourier parameters of this sample to construct a three-dimensional parameter space. The parameters of the Cepheid light curves have to be within this parameter space and are further constrained by a color cut.

In order to find the Cepheids in our data, we apply several selection criteria. From the 3,348,137 resolved sources in the r_{P1} band, we start by selecting those that are also resolved in the i_{P1} band. We also require the source to be periodic in both bands and that the periods are similar to $1\% \left(\left| \frac{P_{P1} - P_{iP1}}{P_{P1}} \right| < 0.01 \right)$. Additionally, we only select sources where the period in the r_{P1} band is $1.5 \text{ days} < P_{P1} < 150 \text{ days}$. The light curves of the resulting 21,313 sources are fitted in order to obtain the Fourier

coefficients A_{21} and φ_{21} . Here A_{21} is the amplitude ratio of the first two Fourier components and φ_{21} is the phase difference between those two coefficients. The Fourier decomposition is done in the same way as described in K13; however, we use less degrees of freedom for the g_{P1} band, i.e., 3 instead of 5. This is because we have less epochs in the g_{P1} band. From the fit, we calculate the mean magnitude by determining the mean flux from the fitted curve and convert the mean flux back to a magnitude. The determination of the error of the mean magnitude is more difficult, since the error is not just the fit error of the mean magnitude. In K13, we used the photometric error determined in the reference frame as the mean magnitude error, since this was the dominating error. While it is still true that the error in the reference frame is the dominating error, we cannot just use this error because the light curve might consist of epochs from multiple reference frames. We determine the mean magnitude error by constructing a sample of 10,000 light-curve realizations. For each realization, we determine the mean magnitude by fitting the corresponding light curve. We construct a new light curve for each realization where each epoch's magnitude is the sum of the flux from the difference frame and a new flux from the corresponding reference frame. This new reference frame flux is drawn from a Gaussian distribution around the measured reference frame magnitude with a width of the measured photometric error. From the distribution of these 10,000 mean magnitudes, we calculate the mean magnitude error. For example, a light curve that consists of data from four different skycells is fitted 10,000 times. Each time, the four reference frame magnitudes are modified by drawing four new magnitudes from four Gaussian distributions with the width of the corresponding reference frame error. In this way, we obtain a new light curve where each epoch's magnitude is modified by changing the corresponding reference frame flux. If the light curve consists almost exclusively of epochs from one skycell, the error of the corresponding reference frame will dominate the mean magnitude error. This is not always the case, however; hence, we have to use this sophisticated procedure to determine the mean magnitude error. We also calculate the errors of A_{21} and φ_{21} simultaneously with calculating the mean magnitude error using the same technique. The errors of A_{21} and φ_{21} determined with this approach are much smaller than the fit errors of the Fourier decomposition. Therefore, we use the errors obtained from the Fourier decomposition, but the other errors are included in the published data (see the Appendix).

The Wesenheit, a reddening-free magnitude (Madore 1976, 1982; Opolski 1983), is defined as in K13:

$$W_i = r_{P1} - R(r_{P1} - i_{P1}), \quad (1)$$

with $R = 3.86$.

The selection criteria described in the next subsections could be performed in any order. The published data also include those light curves that do not make the selection criteria. We performed the cuts in the order described in the next subsections. Therefore, any fit parameters that were calculated after applying a selection criterion or cut are not available for such light curves excluded before performing the corresponding fit.

3.1. Manual Classification

As described previously, we need to identify a certain number of Cepheids manually so that we are able to construct a

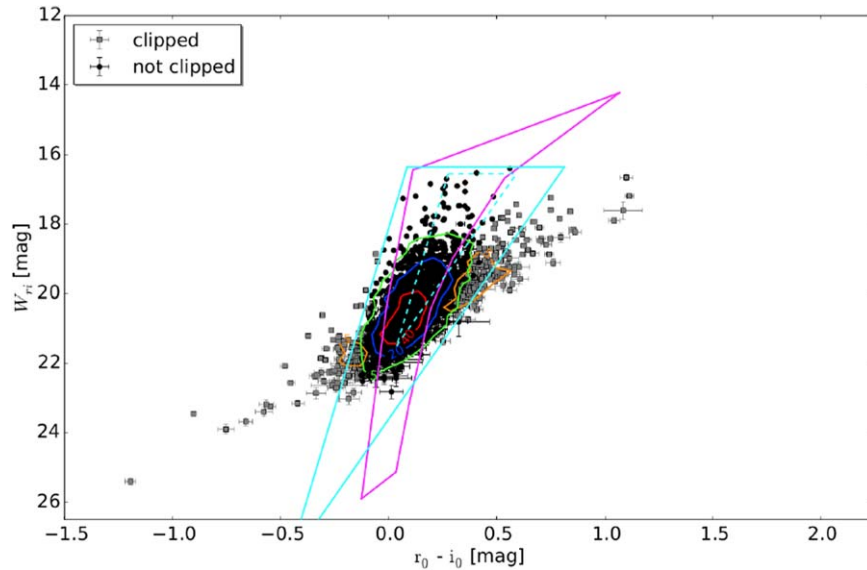


Figure 2. Color–Wesenheit cut for the manually selected Cepheid sample. Four authors independently identified 1966 sources as Cepheids by only considering the shape of the light curve. The color cut shown in Figure 4 is applied to this manually selected sample, and 295 sources are clipped, leaving 1671 Cepheids. The extinction correction is done by using the Montalto et al. (2009) color-excess map. The edges of the instability strip are used to constrain the color-excess estimate. The lines are the same as in Figure 4. The error bars shown are the photometric errors. The possible color-excess range is also considered for the cut; therefore, some points appear to be outside of the region defined by the magenta lines but are still classified as Cepheids. Density contour lines to the selected and clipped sample are also shown.

three-dimensional parameter space that enables us to find Cepheids in as unbiased a way as possible. Of course, the manual selection of Cepheids by light-curve shape is biased to some degree. It is especially difficult to determine the variable type for noisy light curves. As described previously, we start with 21,313 sources but only select those where the period significance determined by SigSpec is larger than 25. This leaves us with 10,562 light curves. From these, we preselected 2807 by using only those that are not noisy, and the light curves that even remotely resemble Cepheids, i.e., Mira-like light curves, were also selected. The selection is only based on the shape of the light curves in all available bands. So, we do not look at the position in the PLR. In order to be as unbiased as possible, four of the authors independently assigned flags to those 2807 light curves. We then matched the four classifications and reviewed cases where we disagreed. We disregarded sources where we could not reach a consensus of opinion. We end up with 1966 light curves that are manually classified as Cepheids based only on their light-curve shape. We apply the color cut described in the next subsection and clip 295 sources, leaving us with 1671 Cepheids. The color cut can be seen in Figure 2. The number of clipped sources is quite high considering that they were manually identified to have a Cepheid-like light curve. The color cut used in K13, shown with cyan lines, would cut less objects, but the new color cut (magenta lines) works better in selecting Cepheids in the complete sample.

3.2. Instability Strip Cuts

As already mentioned, we use a color cut for a better identification of Cepheids. We use the reddening-free Wesenheit and the $r_{P1} - i_{P1}$ color for the selection, since we do not have g_{P1} data for all light curves. In order to define the color cut, we use the same approach as in K13. Theoretical pulsation models provide us with the information on how the instability strip edges depend on the effective temperature (T_{eff}) and

luminosity (L). We then use isochrones to translate the instability strip defined by T_{eff} and L to the observable color and Wesenheit. In K13, we used the Fiorentino et al. (2002) instability strip but had to extend the edges by 0.2 mag in order to also include fainter but obvious Cepheids that would otherwise not have been covered, which makes the reliability of the instability strip parameters somewhat doubtful. Now we use the Anderson et al. (2016) instability strip edge models. As can be seen in Figure 3, those also include fainter and cooler Cepheids. We include all their models from Tables A.1 to A.6, i.e., all three metallicities ($Z = 0.014, 0.006, \text{ and } 0.002$) and all three rotations ($\omega_{\text{ini}} = 0.0, 0.5, \text{ and } 0.9$). The Anderson et al. (2016) instability strip edges are used to define an area in which we require our Cepheids to reside. The area is defined by lines connecting the points (3.755, 4.8), (3.890, 1.5), (3.550, 4.8), (3.740, 2.934), and (3.812, 1.5), as shown in Figure 3. In the next step, we use the PARSEC isochrones (Bressan et al. 2012; Chen et al. 2014, 2015; Tang et al. 2014) and require the T_{eff} and L of the isochrones to be within the area defined by the instability strip edges. This defines an area in the Wesenheit–color diagram, as seen in Figure 4. This region, which is defined by lines connecting the points (0.111, 16.450), (−0.010, 20.350), (−0.126, 25.900), (0.033, 25.134), (0.092, 23.222), (0.194, 20.430), (0.294, 19.003), (0.536, 16.680), and (1.067, 14.223), is used to perform the color cut. The area shown in Figure 4 is also valid for all metallicities used in the Anderson et al. (2016) models. In order not to clutter up the plot, we only show the solar-metallicity isochrones. The isochrones can also be used to determine the instability strip in other filter bands. We use this in K18b, where we identify our Cepheid sample in *HST* data. Since the color cut uses the intrinsic color, we have to correct for the extinction. As in K13, we use the Montalto et al. (2009) color-excess map and the foreground extinction toward M31 determined by Schlegel et al. (1998) ($E(B - V)_{\text{fg}} = 0.062$) combined with the correction factor 0.86 from Schlafly & Finkbeiner (2011). The

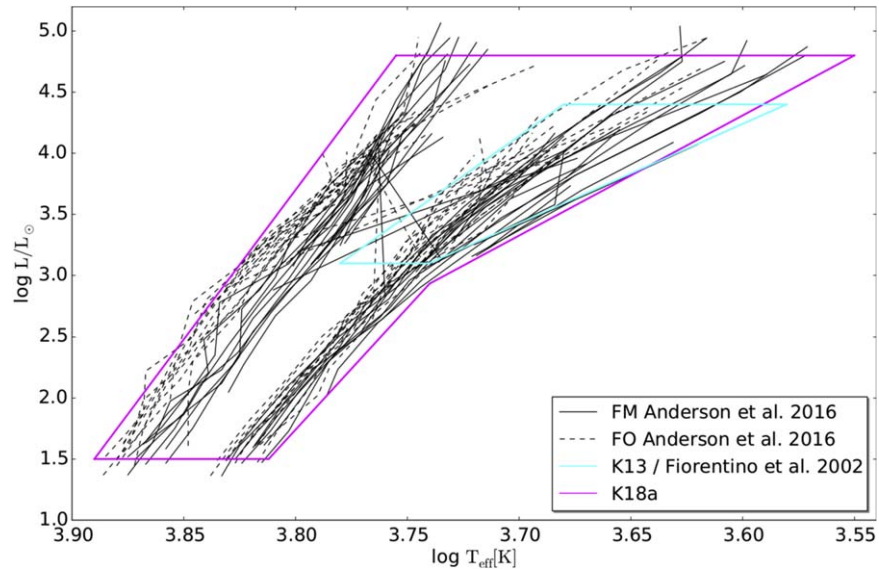


Figure 3. Instability strip edges used to perform the color–Wesenheit cut. The outline of the region used in K13 (cyan line) is based on the Fiorentino et al. (2002) instability strip. All Anderson et al. (2016) instability strip edge models contained in their Tables A.1–A.6 are shown in black. This implies that we show all three metallicities ($Z = 0.014, 0.006,$ and 0.002) and rotations ($\omega_{\text{ini}} = 0.0, 0.5,$ and 0.9). The FM models are shown as solid lines and the FO models as dashed lines. The magenta outlined region that we use for the color–Wesenheit cut was chosen such that it encompasses the Anderson et al. (2016) models while keeping the shape of the region as simple as possible. The region is defined by straight lines connecting the points (3.755, 4.8), (3.890, 1.5), (3.550, 4.8), (3.740, 2.934), and (3.812, 1.5).

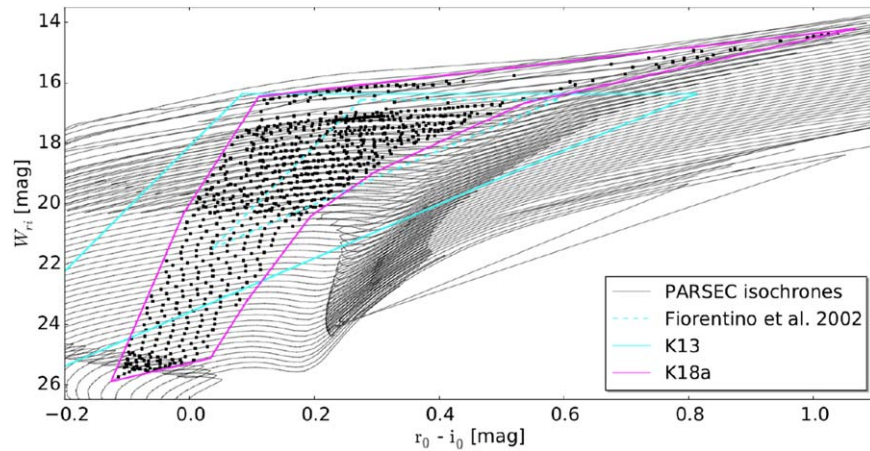


Figure 4. Instability strip region used for the color–Wesenheit cut. The area enclosed by the dashed cyan triangle is defined by the Fiorentino et al. (2002) instability strip. In K13, we had to enlarge this region by 0.2 mag in all directions. The resulting region, defined by the solid cyan lines, also covers fainter Cepheids that would be cut if the dashed cyan triangle were used. The PARSEC isochrones (Bressan et al. 2012; Chen et al. 2014, 2015; Tang et al. 2014), shown in black, have solar metallicity ($Z = 0.0152$) and ages in the range $7.05 \leq \log(\text{age yr}^{-1}) \leq 9.25$ and have been shifted by a distance modulus of 24.36 mag (Vilardell et al. 2010). The black squares show where the luminosity and temperature of the isochrones are within the magenta area defined in Figure 3. These points define the magenta outlined region that is used to perform the color cut. For visibility reasons, this plot only shows the isochrones with solar metallicity, but the magenta outlined region is chosen such that it also encompasses the other two metallicities from the Anderson et al. (2016) models. The color–Wesenheit cut region is defined by straight lines connecting the points (0.111, 16.450), (−0.010, 20.350), (−0.126, 25.900), (0.033, 25.134), (0.092, 23.222), (0.194, 20.430), (0.294, 19.003), (0.536, 16.680), and (1.067, 14.223).

Montalto et al. (2009) map gives the color excess for a line of sight going completely through M31. Therefore, we only correct by half the color excess, assuming the Cepheid is only affected by half the dust. This corresponds to a probability argument, where sources are in front of an infinitely thin dust layer or behind, e.g., the extinction correction in the r_{P1} band, as

$$\overline{A_{r_{P1}}} = (0.5 \cdot E(B - V) + 0.86 \cdot 0.062) \cdot R_{r_{P1}}, \quad (2)$$

where $R_{r_{P1}} = 2.5535$ ($R_{i_{P1}} = 1.8928$ and $R_{g_{P1}} = 3.5258$) for a reddening law of $R_V = 3.1$. The assumption that the Cepheid is obscured by only half the dust can be refined in some cases. An

object satisfies the color selection if it is within the area defined above, also considering its errors. So each object is not a point in the Wesenheit–color space but rather a box, where the height of the box is the error of the Wesenheit. The width of this box is the error of the color combined with the full color excess of that object. So the right side of the box is where only the foreground extinction has been corrected, and the left side is where the foreground plus the full color excess is used. In an edge-on view this corresponds to a location on the top of the disk, where only the foreground extinction has to be considered, or the bottom, where additionally the full color excess has to be taken into account. In case this box intersects

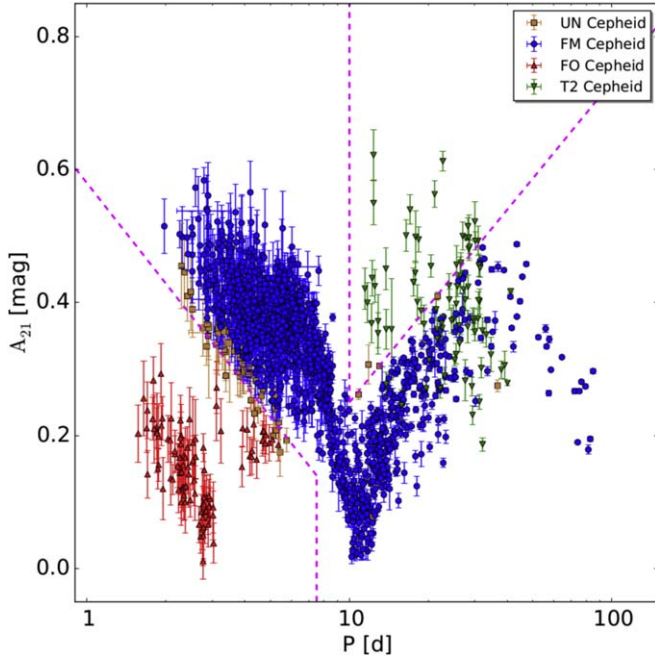


Figure 5. Amplitude ratio (A_{21}) diagram for the manually classified Cepheid sample. This projection of the three-dimensional space is mainly used to identify the FO Cepheids, but there is also a region that is used to classify a part of the T2 Cepheids. The region used to identify the FO Cepheids (Equations (9) and (10)) is marked with dashed magenta lines. Also, the T2 region (Equations (14) and (15)) is marked with dashed magenta lines. In total, there are 54 UN Cepheids, 1401 FM Cepheids, 103 FO Cepheids, and 82 T2 Cepheids.

the color-cut area defined by the instability strip edges, half the width of the box that is inside the color-cut area and is due to the color excess is used to correct the extinction. So we use the color-cut area to narrow down the range of color excess the object can have.

In the following, we use the extinction-corrected magnitudes, i.e., r_{P1} denotes the extinction-corrected magnitude. The uncertainty caused from the color excess is not propagated into the magnitude errors.

3.3. Type Classification

Fundamental-mode (FM) and first-overtone (FO) Cepheids, as well as type II (T2) Cepheids, occupy different locations in the $A_{21}-\varphi_{21}-P$ space, which can be used to identify the Cepheid type (see, e.g., Udalski et al. 1999; Vilardell et al. 2007; K13). As in K13, we use two projections of this space, i.e., $A_{21}-P$ (see Figure 5) and $\varphi_{21}-P$ (see Figure 6), for the type classification. In K13, we used the $A_{21}-P$ projection to distinguish between FM and FO Cepheids and the $\varphi_{21}-P$ space to separate T2 and FM Cepheids. Here we additionally use an area in the $\varphi_{21}-P$ projection to find T2 Cepheids. The different Cepheid types could also be identified in the PLR, but by using this three-dimensional space, i.e., using the Fourier parameters, we only use the light-curve shape to determine the Cepheid type. The FO and FM PLRs have a small separation compared to their dispersions. Therefore, defining a line in the PLR that would distinguish both Cepheid types would bias the resulting PLRs. In the three-dimensional Fourier space, we also see overlaps between the different Cepheid type sequences. To address this issue, we require the Cepheids to be completely

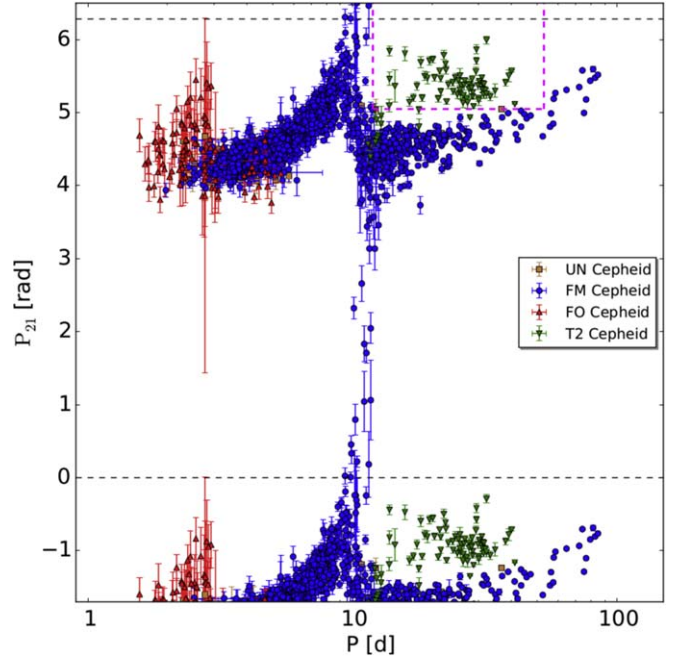


Figure 6. Phase difference (φ_{21}) diagram for the manually classified Cepheid sample. This projection of the three-dimensional space is used to identify the bulk of the T2 Cepheids. The region used for this classification (Equations (11)–(13)) is marked with dashed magenta lines. Here φ_{21} is 2π periodic; therefore, the data between the dashed black lines are also plotted periodic for better visibility. The number of Cepheids in each subtype is the same as in Figure 5.

inside the defined areas, including their errors. Consequently, some Cepheids are in a transition region and therefore cannot be assigned a definite Cepheid type. We label those as the unclassified (UN) Cepheid type. In K13, we called the Cepheids that were clipped in the Wesenheit relation UN Cepheids. As we will discuss later, we still perform outlier clipping in the Wesenheit PLR and call the clipped Cepheids UN Cepheids. Therefore, in this paper, UN Cepheids can arise from two reasons. We do not distinguish between the two and call both UN Cepheids. We separate the areas by defining the following linear parameterization:

$$m_{\text{FO}} = \frac{0.14 - 0.34}{\log(7.5) - \log(3.0)}, \quad (3)$$

$$t_{\text{FO}} = 0.34 - \log(3.0) \cdot m_{\text{FO}}, \quad (4)$$

$$m_{\text{T2,1}} = 0.00, \quad (5)$$

$$t_{\text{T2,1}} = 5.05, \quad (6)$$

$$m_{\text{T2,2}} = \frac{0.48 - 0.25}{\log(30.0) - \log(10.0)}, \quad (7)$$

and

$$t_{\text{T2,2}} = 0.25 - \log(10.0) \cdot m_{\text{T2,2}}. \quad (8)$$

In order for a Cepheid to be assigned the FO type, the following two equations have to be true (see Figure 5):

$$A_{21} + A_{21,e} < \log(P) \cdot m_{\text{FO}} + t_{\text{FO}} \quad (9)$$

and

$$P < 7.5 \text{ days}. \quad (10)$$

Table 1
Selection Criteria Used in the r_{P1} and i_{P1} Bands

| Band | Selection Criterion | Manual | 3D | Flag |
|------|-----------------------|--|-----------|------|
| I | All | 295/1966 | 1922/3390 | 1 |
| II | r_{P1} and i_{P1} | 15 mag $\leq m(t) \leq$ 25 mag | 0/1468 | 2 |
| III | r_{P1} and i_{P1} | $0.1 \text{ mag} \leq \max(m(t)) - \min(m(t)) \leq$ 1.75 mag | 1/1468 | 4 |
| IV | r_{P1} and i_{P1} | $\frac{\text{median}(m(t) - m_i)}{\max(m(t)) - \min(m(t))} \leq$ 0.3 | 20/1468 | 8 |
| V | r_{P1} and i_{P1} | $\max(\Theta_i - \Theta_{i+1}) \leq$ 0.25 | 0/1468 | 16 |
| VI | All | Same type from light-curve bootstrap \geq 90% | 3/1468 | 32 |
| | r_{P1} and i_{P1} | Final sample | 1640 | 1046 |

Note. The number of remaining Cepheids for the manual and 3D sample does not have to add up to the final number, since some cuts are performed at the same time and some objects fulfill multiple criteria. The columns Manual and 3D provide the number of clipped objects and the total number of objects still present at this step. The Flag column provides a bit flag so that the reason for the clipping can be found in the published data. The magnitude of the fitted light curve is denoted as $m(t)$, while the observed magnitudes are called m_i . Here Θ_i is the phase of the i th observed epoch, and Θ_{i+1} is the next largest phase (which is not necessarily the next epoch).

Table 2
Selection Criteria Used in the g_{P1} Band, Otherwise See Table 1

| Band | Selection Criterion | Manual | 3D | Flag |
|------|---------------------|--|-----------|------|
| I | All | 295/1966 | 1922/3390 | 1 |
| II | g_{P1} | 15 mag $\leq m(t) \leq$ 25 mag | 162/1468 | 2 |
| III | g_{P1} | $0.1 \text{ mag} \leq \max(m(t)) - \min(m(t)) \leq$ 2.00 mag | 198/1468 | 4 |
| IV | g_{P1} | $\frac{\text{median}(m(t) - m_i)}{\max(m(t)) - \min(m(t))} \leq$ 0.3 | 24/1468 | 8 |
| V | g_{P1} | $\max(\Theta_i - \Theta_{i+1}) \leq$ 0.25 | 175/1468 | 16 |
| VI | All | Same type from light-curve bootstrap \geq 90% | 3/1468 | 32 |
| | g_{P1} | Final sample | 1302 | 595 |

For it to be a T2 Cepheid, the equations (see Figure 6)

$$P > 11.95 \text{ days}, \quad (11)$$

$$\varphi_{21} - \varphi_{21,e} > \log(P) \cdot m_{T2,1} + t_{T2,1}, \quad (12)$$

and

$$P < 53.0 \text{ days} \quad (13)$$

or the equations (see Figure 5)

$$A_{21} - A_{21,e} > \log(P) \cdot m_{T2,2} + t_{T2,2} \quad (14)$$

and

$$P > 10.0 \text{ days} \quad (15)$$

have to be true, i.e., (Equation (11) AND Equation (12) AND Equation (13)) OR (Equations (14) AND (15)). For it to be considered an FM Cepheid, at least one of the equations (see Figure 5)

$$A_{21} - A_{21,e} > \log(P) \cdot m_{FO} + t_{FO} \quad (16)$$

and

$$P > 7.5 \text{ days} \quad (17)$$

has to be true, and additionally, at least one of the equations (see Figure 6)

$$P < 11.95 \text{ days}, \quad (18)$$

$$\varphi_{21} + \varphi_{21,e} < \log(P) \cdot m_{T2,1} + t_{T2,1}, \quad (19)$$

and

$$P > 53.0 \text{ days} \quad (20)$$

has to be true. Also, at least one of the equations (see Figure 6)

$$A_{21} + A_{21,e} < \log(P) \cdot m_{T2,2} + t_{T2,2} \quad (21)$$

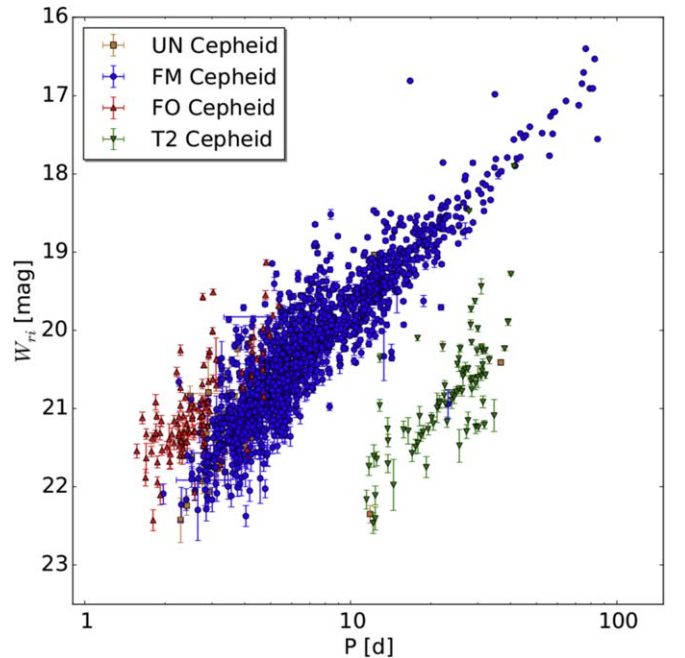


Figure 7. Period Wesenheit diagram for the manually classified Cepheid sample. At this point, no outlier clipping has been performed. Therefore, all UN Cepheids are due to uncertainties in the type classification. The number of Cepheids in each subtype is the same as in Figure 5. Considering the dispersion in each relation, the type classification performs well. The PLRs are well sampled, and no obvious selection effects from the manual classification that is based on the shape of the light curve can be seen.

and

$$P < 10.0 \text{ days}. \quad (22)$$

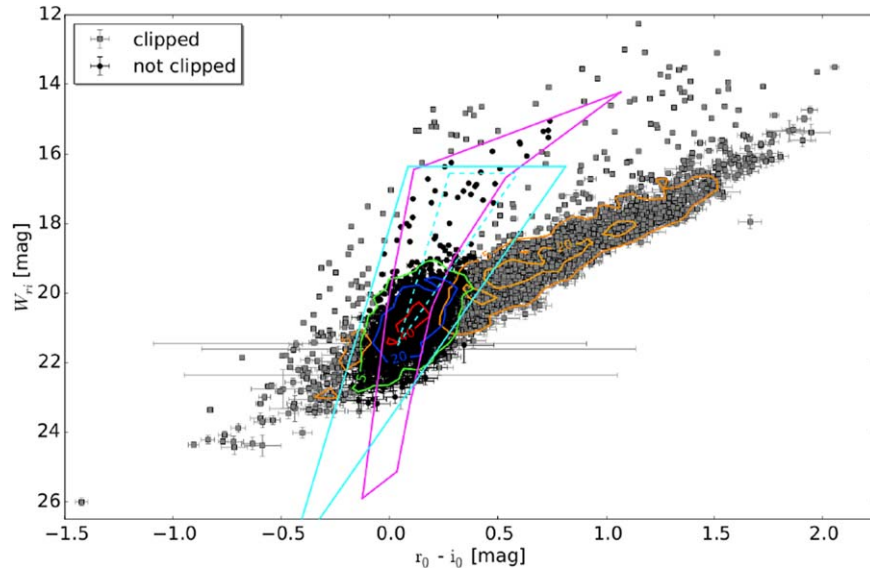


Figure 8. Color–Wesenheit cut for the Cepheid sample selected by the 3D parameter space. Here 3390 light curves are selected by the 3D parameter space classification. As for Figure 2, the color cut is applied and 1922 sources are clipped, with 1468 sources remaining after the color cut. The extinction correction is done by using the Montalto et al. (2009) color-excess map. The edges of the instability strip are used to constrain the color-excess estimate. The lines are the same as in Figure 4. The error bars shown are the photometric errors. The possible color-excess range is also considered for the cut; therefore, some points appear to be outside of the region defined by the magenta lines but are still classified as Cepheids.

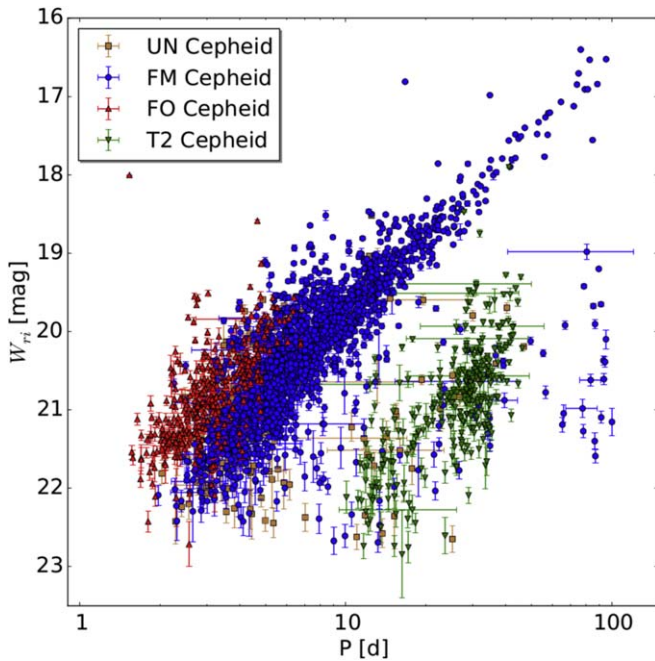


Figure 9. Period Wesenheit diagram for the complete sample (i.e., the manual sample combined with the 3D sample) without outlier clipping. All UN Cepheids are due to uncertainties in the type classification. Most outliers are due to misclassification and crowding. In total, there are 203 UN Cepheids, 1851 FM Cepheids, 331 FO Cepheids, and 301 T2 Cepheids.

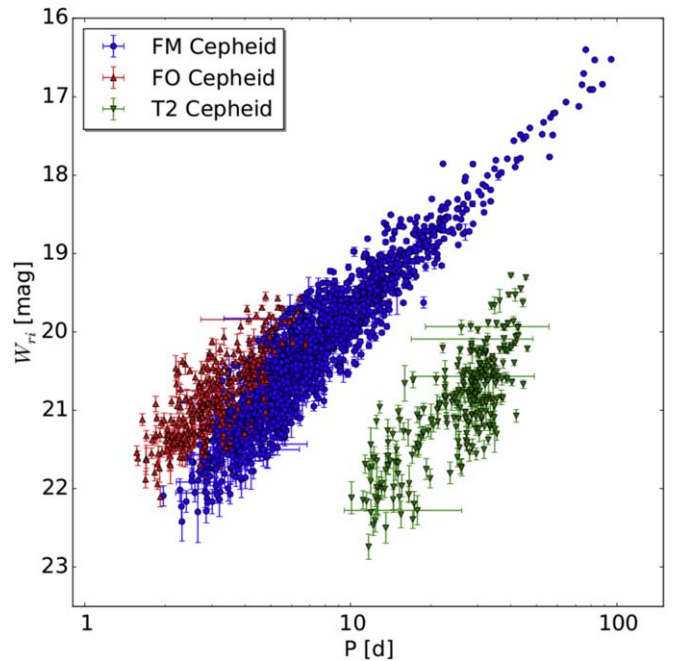


Figure 10. Period Wesenheit diagram for the complete sample after the outlier clipping. The outlier clipping was performed with the method we developed in K15. As can be seen, the outliers still present in Figure 9 are clipped. In total, there are 1662 FM Cepheids, 307 FO Cepheids, and 278 T2 Cepheids.

has to be true; i.e., for an FM Cepheid, the logical connection is (Equation (16) OR Equation (17)) AND (Equations (18) OR Equation (19) OR Equation (20)) AND (Equation (21) OR Equation (22)). In case the Cepheid cannot be classified as FM, FO, or T2, it is classified as UN. Figure 7 shows that the type classification of the manually selected Cepheid sample performs reasonably well considering the dispersion in the PLRs.

3.4. Selection Criteria

In order to facilitate the automatic classification of Cepheids, additional selection criteria are needed. The combination of color cut and three-dimensional parameter space selection alone does not suffice to obtain a clean Cepheid sample. Table 1 summarizes the selection criteria and provides information on how many objects are rejected in each step. The cuts could be applied in any order without changing the

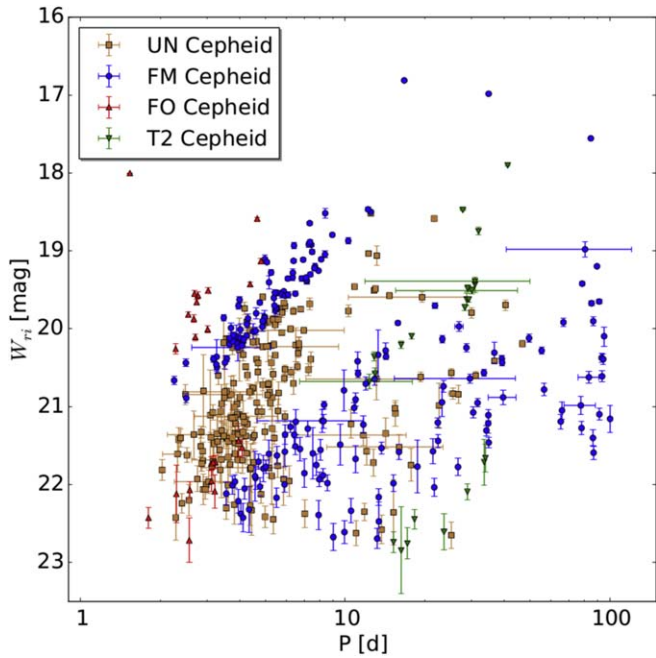


Figure 11. Period Wesenheit diagram of the Cepheids clipped from the complete sample. The UN Cepheids shown here are due to uncertainties in the type classification. All Cepheids shown in this plot are assigned the UN type after the clipping is performed, and we do not distinguish between the two reasons for a UN Cepheid (type classification and clipping) anymore. Shown are 203 UN Cepheids, 189 FM Cepheids, 24 FO Cepheids, and 23 T2 Cepheids.

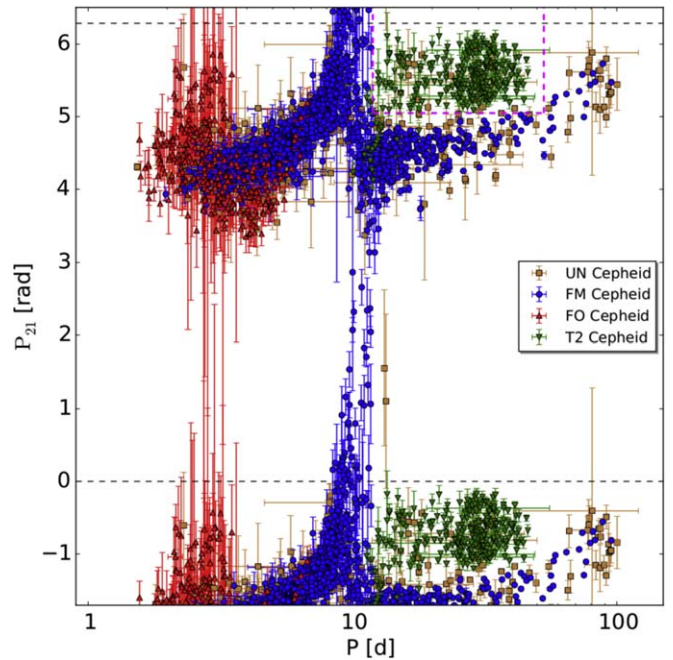


Figure 13. Phase difference (φ_{21}) diagram for the final sample. Similar to Figure 12, this projection of the 3D parameter space is also more densely populated than in the manual sample shown in Figure 6. The dashed magenta lines are the same as in Figure 6 and also used to determine the Cepheid type. The data between the black dashed lines are periodic and therefore also plotted periodic. The number of Cepheids is the same as in Figure 12.

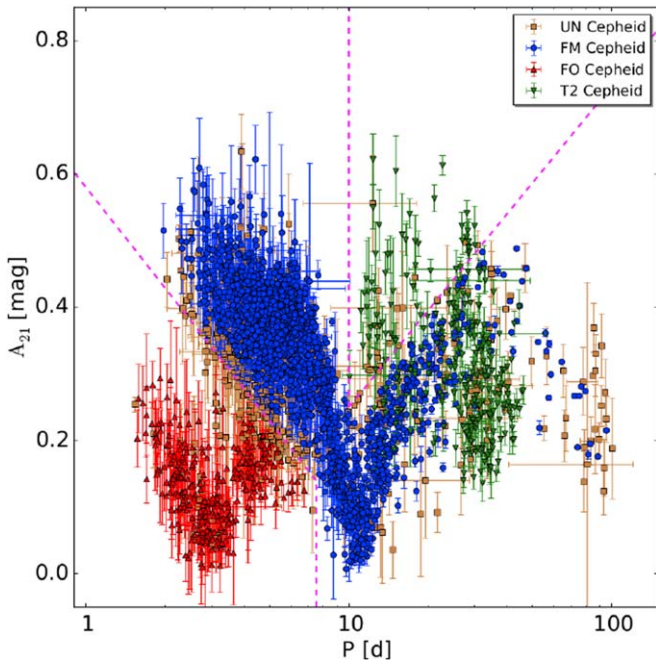


Figure 12. Amplitude ratio (A_{21}) diagram for the final sample. The parameter space is better sampled than for the manual sample in Figure 5. The shape of the 3D parameter space projection is similar to that of the manual sample, since the additional Cepheids have been selected using this parameter space. The dashed magenta lines are the same as in Figure 5 and are used for the type classification. In total, there are 439 UN Cepheids, 1662 FM Cepheids, 307 FO Cepheids, and 278 T2 Cepheids.

resulting sample. The published Cepheid catalog also includes the tables and light curves of the clipped objects, as well as information on the clipping reason in the form of a bit flag.

Some fits or, e.g., the final type determination are performed after certain cuts have been applied in order to save computation time. Therefore, the catalog of the clipped objects might not have all the information. The selection criteria are applied to the manually classified Cepheid sample, as well as the sample that is selected using the three-dimensional parameter space (3D sample). Table 1 provides the number of clipped objects for each sample. The selection criteria are applied first to the manual sample so that the three-dimensional parameter space can be defined (as explained in the next section). The selection criteria are then applied again to the resulting 3D sample. The selection criteria in Table 1 are applied to the r_{P1} and i_{P1} bands, while the criteria in Table 2 are applied to the g_{P1} band. Objects clipped due to the criteria in Table 1 are removed from the final Cepheid sample, while objects clipped only in the g_{P1} band (Table 2) are flagged and therefore not used for the g_{P1} PLR or the g_{P1} sample in general.

Criterion I, the color cut discussed previously, is an important selection criterion for the 3D sample. Selection criterion II is a magnitude cut that ensures that the fitted light curve does not overshoot. As can be seen in Table 1, this cut is not used for the r_{P1} and i_{P1} band, but the cut is relevant for the g_{P1} band (Table 2). This is not surprising, since the g_{P1} band has relatively few epochs, and the light curves therefore have gaps that facilitate overshoots in the light-curve fitting. Criterion III is an amplitude cut, where we reject small amplitudes because those are difficult to distinguish from noise. Amplitudes are smaller for longer wavelengths (Madore & Freedman 1991), and therefore we have a different upper amplitude cut in the g_{P1} band. In criterion IV, we make a noise cut by comparing the median absolute deviation of the observed magnitudes with the fitted magnitudes in relation to the amplitude of the light curve. Large gaps in the light curve

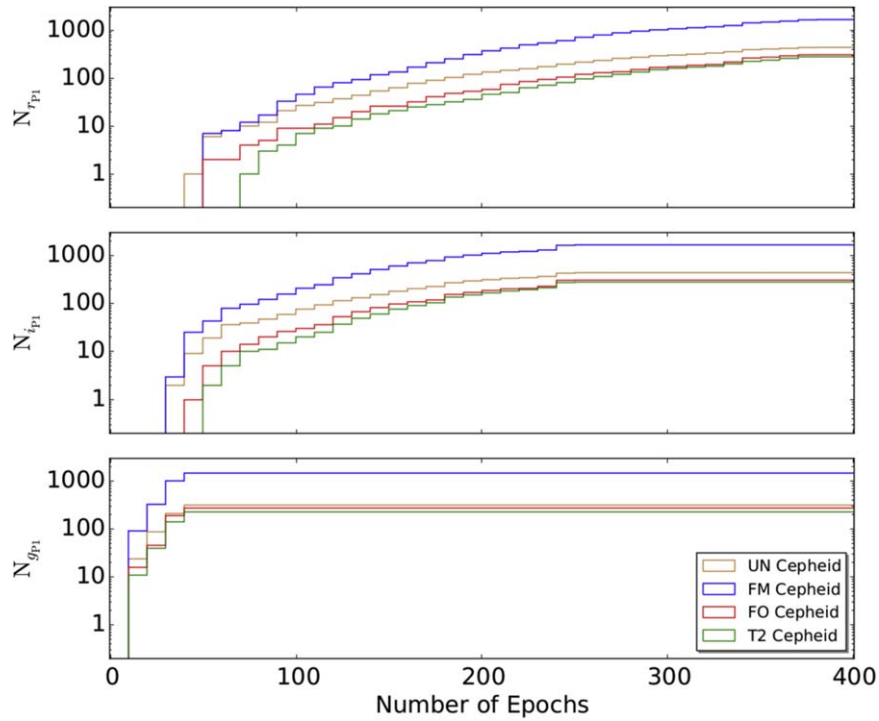


Figure 14. Cumulative histogram of the epoch distribution for the r_{P1} , i_{P1} , and g_{P1} bands of the PAndromeda Cepheid catalog. The bin size is 10 epochs. In total, the PAndromeda data consist of up to 420 epochs in the r_{P1} band, up to 262 epochs in the i_{P1} band, and up to 56 epochs in the g_{P1} band. As can be seen, these numbers are not reached because we require the Cepheid epochs in the light curves to have a signal-to-noise ratio of larger than two and a visit stack depth of more than two frames.

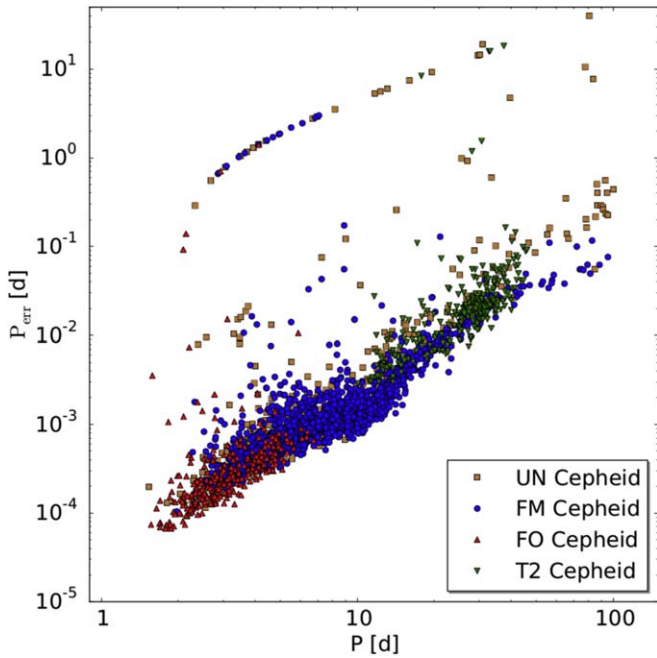


Figure 15. Period error diagram. The period errors are determined through the bootstrapping method. The sequence with the larger period errors is caused by aliasing. The period errors are very small, since the PAndromeda Cepheid sample has a lot of epochs.

cause problems in fitting the light curve. As mentioned previously, the gaps might cause overshoots, but even without overshoots, the shape of the light curve might not be determined well enough for the type classification or the determination of the Fourier parameters A_{21} and φ_{21} . Therefore,

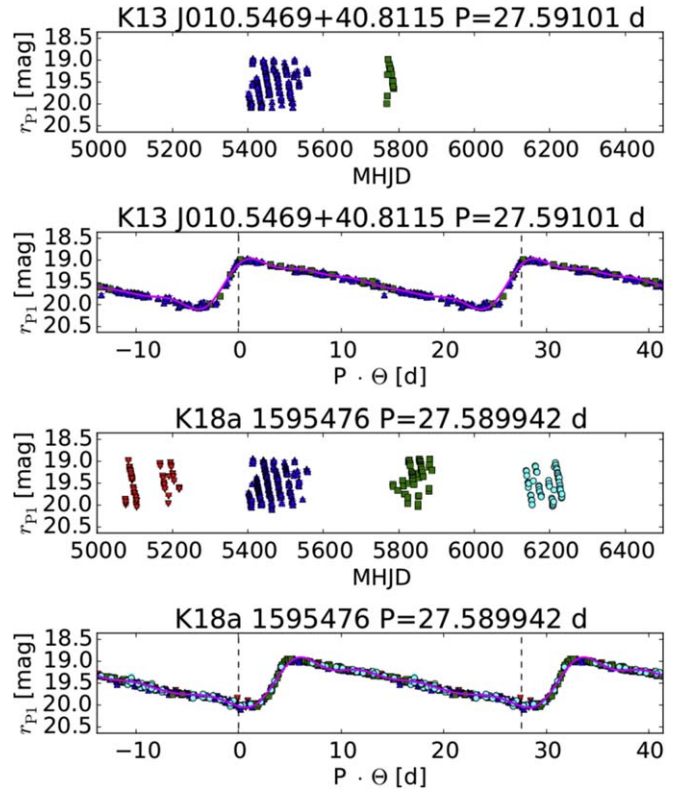


Figure 16. Example light curve of an FM Cepheid in the r_{P1} band. The two upper panels show the K13 data, and the two bottom panels show the new data. Each upper panel of the two samples shows the unfolded light curve with the modified Heliocentric Julian Date on the x axis. Each bottom panel shows the folded light curve and the fit to the light curve as a magenta line. Here the x axis is the product of the period with the phase Θ . The zero point of the phase is arbitrary. Each season's observations are marked in a different color.

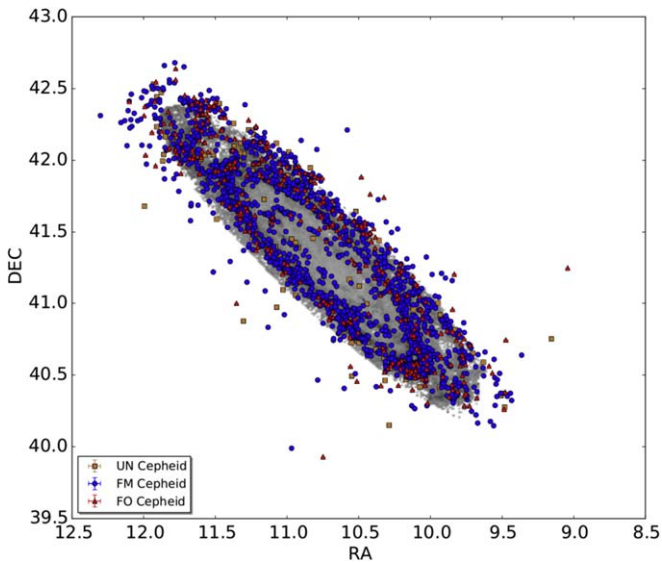


Figure 17. Spatial distribution of FM and FO Cepheids of the PAndromeda Cepheid catalog. The Cepheids are plotted over the $E(B - V)$ map of Montalto et al. (2009), and they follow the ring structure of M31.

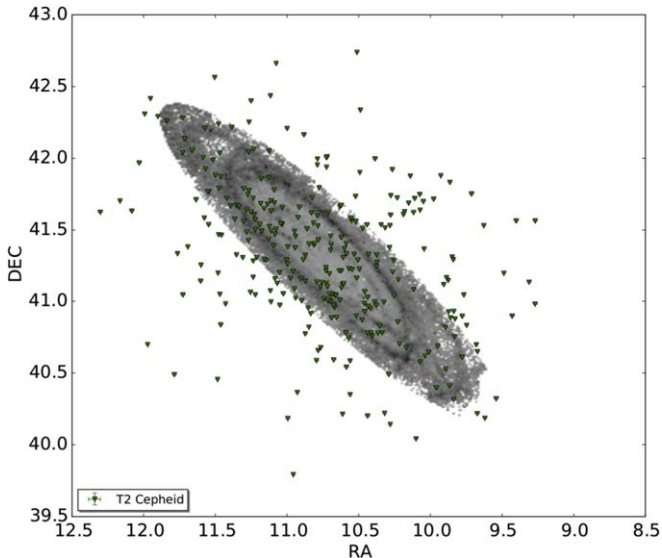


Figure 18. Spatial distribution of T2 Cepheids of the PAndromeda Cepheid catalog. As in Figure 17, the Cepheids are plotted over the Montalto et al. (2009) $E(B - V)$ map. In contrast to the FM and FO Cepheids, the T2 Cepheids follow the M31 halo.

we introduce criterion V, where we require that the largest gap is smaller than a quarter phase of the light curve. As we mentioned previously, we perform 10,000 bootstrapping realizations for determining the magnitude error and the errors of the Fourier parameters A_{21} and φ_{21} . For each of those realizations, we determine the Cepheid type and require in criterion VI that the Cepheid type is the same in more than 9000 realizations. There are also two additional flags (64 and 128) not mentioned in Tables 1 and 2. Flag 64 is assigned to seven manually classified Cepheids, and they are removed from the Cepheid sample because of their location in the 3D parameter space. The reason for this is explained in the next subsection. Flag 128 is assigned 19 times in the final Cepheid catalog (so those Cepheids are still included in the catalog) in

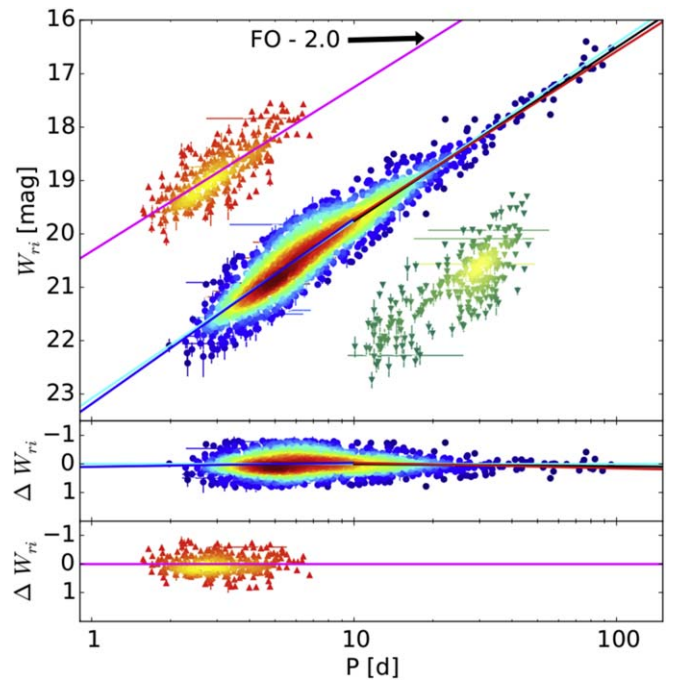


Figure 19. Period Wesenheit diagram. In total, there are 1662 FM Cepheids, 307 FO Cepheids, and 278 T2 Cepheids. In the top panel, the FO Cepheids have been shifted by 2 mag for better visibility. The FM Cepheids are shown as circles, the FO Cepheids are shown as upward-pointing triangles, and the T2 Cepheids are shown as downward-pointing triangles. The color is assigned according to the density of Cepheids in this part of the PLR by using the kernel density estimate. The cyan line corresponds to fit #1 in Table 3, while the black line is fit #2 (only long-period Cepheids). The magenta line is fit #3 in the same table. The blue and red lines are from the broken-slope fit #1 in Table 4. The two bottom panels show the residuals of the fit to the cyan and magenta lines, respectively.

order to mark Cepheids where the light curve from visual inspection does not look like a typical Cepheid light curve. We keep those Cepheids in the sample so that the selection of Cepheids is as objective as possible. The results do not change if we disregard those Cepheids.

3.5. 3D Classification

Similar to K13, we use the 3D parameter space $A_{21}-\varphi_{21}-P$ to select light curves that have a shape typical for a Cepheid. The advantages of this approach are that it is less biased than visual selection and the selection is reproducible. Nevertheless, the approach requires the manual sample in order to define this 3D space. In K13, we spanned a grid in this 3D space and selected those grid points where one manually classified Cepheid resides. By doing this, we had to choose six parameters, i.e., the grid size and starting point for each dimension. Here we improve the method by using only three parameters. We define a sphere around each point in the manual sample. In order for an object to be selected, it has to be inside at least one of the spheres that are made up by the manual sample in the $A_{21}-\varphi_{21}-P$ space. One of the free parameters is the radius of the sphere, and the other two are the normalizations of the other two dimensions, i.e., how each dimension is scaled compared to the other dimensions. We choose $A_{21}-(2\pi)^{-1}\varphi_{21}-\log(P)$ as the new 3D space. We choose it such that the values of the manual sample have a similar range. The reason for this is that we can use a sphere and do not have to use an ellipsoid. For example, if we use a radius of 0.2 in $A_{21}-\varphi_{21}-P$ space, that

Table 3
PLR Fit Parameters

| # | Band | Type | Range | N_{fit} | a ($\log P = 1$) | Slope b | σ |
|----|-----------|------|---------------|------------------|----------------------|----------------|----------|
| 1 | Wesenheit | FM | All | 1662 | 19.752 (0.008) | -3.323 (0.026) | 0.327 |
| 2 | Wesenheit | FM | $\log(P) > 1$ | 422 | 19.760 (0.020) | -3.247 (0.058) | 0.265 |
| 3 | Wesenheit | FO | All | 307 | 19.256 (0.071) | -3.065 (0.131) | 0.317 |
| 4 | r_{P1} | FM | All | 1662 | 20.371 (0.011) | -2.548 (0.035) | 0.354 |
| 5 | r_{P1} | FM | $\log(P) > 1$ | 422 | 20.365 (0.028) | -2.443 (0.105) | 0.398 |
| 6 | r_{P1} | FO | All | 307 | 19.811 (0.065) | -2.456 (0.115) | 0.259 |
| 7 | i_{P1} | FM | All | 1662 | 20.212 (0.009) | -2.749 (0.029) | 0.304 |
| 8 | i_{P1} | FM | $\log(P) > 1$ | 422 | 20.210 (0.023) | -2.651 (0.083) | 0.322 |
| 9 | i_{P1} | FO | All | 307 | 19.667 (0.060) | -2.615 (0.105) | 0.243 |
| 10 | g_{P1} | FM | All | 1298 | 20.822 (0.018) | -2.202 (0.058) | 0.433 |
| 11 | g_{P1} | FM | $\log(P) > 1$ | 289 | 20.843 (0.051) | -2.186 (0.262) | 0.533 |
| 12 | g_{P1} | FO | All | 246 | 20.319 (0.087) | -1.997 (0.152) | 0.298 |

Note. The magnitude errors were set to the same value. The errors of the fitted parameters were determined with the bootstrapping method.

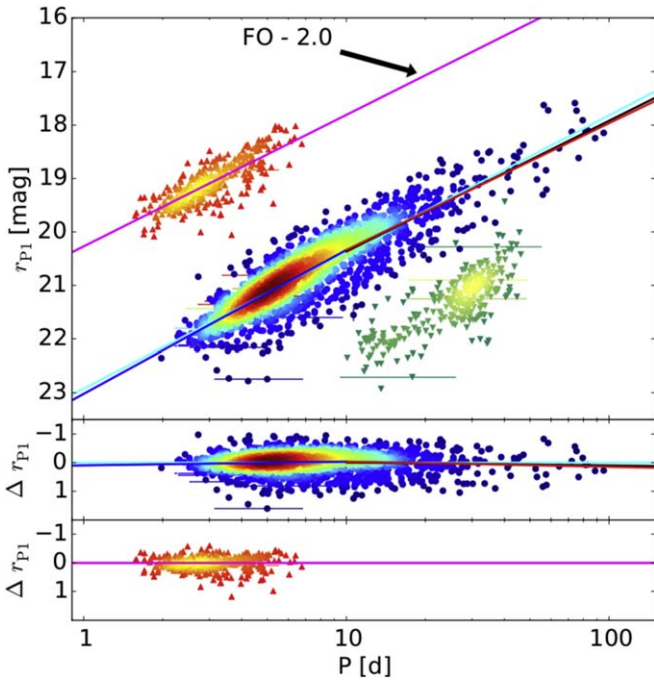


Figure 20. The r_{P1} -band PLR. The number of Cepheids is the same as in Figure 19. The FO Cepheids have been offset by 2 mag for better visibility. The FM Cepheids are shown as circles, the FO Cepheids are shown as upward-pointing triangles, and the T2 Cepheids are shown as downward-pointing triangles. The FM Cepheid PLR is shown as a cyan line and corresponds to fit #4 in Table 3. The fit to the long-period FM Cepheids is shown as a black line (fit #5 in Table 3), while the FO Cepheid PLR is shown as a magenta line (fit #6 in Table 3). The blue and red lines are the fit of a broken slope with a common suspension point, shown as fit #2 in Table 4. As in Figure 19, the two bottom panels show the residuals to fits #4 and #6 in Table 3, respectively.

would be a large difference in A_{21} , while it is only a small change in φ_{21} and almost no change in P . In order to determine the radius of the sphere, we use the manual sample. We calculate for each Cepheid in the manual sample the distance in $A_{21} - (2\pi)^{-1} \varphi_{21} - \log(P)$ space to the next closest Cepheid. The cumulative distribution function of this distance is then used to choose the radius of the sphere. We select a radius of 0.088 for the sphere (99.5% of Cepheids are closer than this distance to their next neighbor). Seven Cepheids have a larger distance to the next neighbor. We choose to cut those seven Cepheids because they are in a region of the 3D space that is sparsely

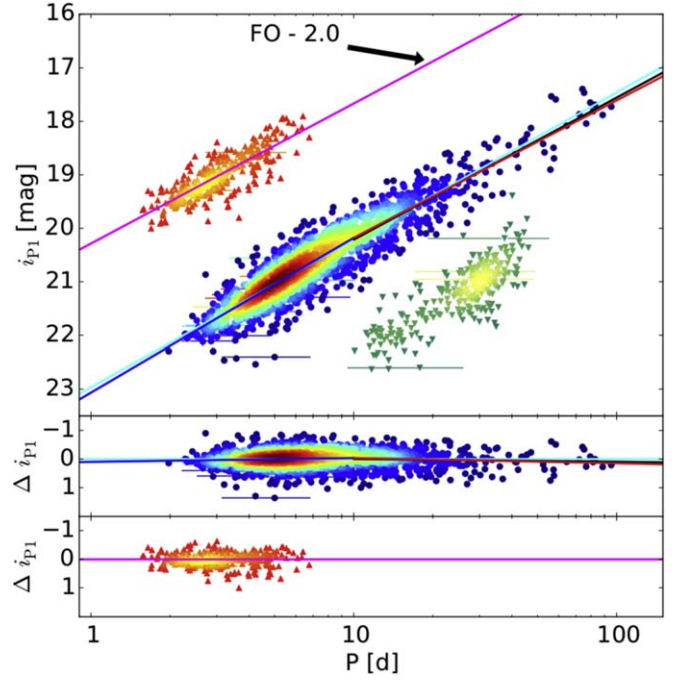


Figure 21. The i_{P1} -band PLR. Shown are fits #7, #8, and #9 from Table 3 and fit #3 from Table 4. Otherwise, the figure is analog to Figures 19 and 20.

sampled, and if they were to be included, the radius of the sphere would have to be increased significantly, which makes the selection worse (a larger radius means a more fuzzy selection). If the seven Cepheids were left in the sample but the 0.088 radius were used, then the seven Cepheids would be rejected by the 3D selection process if the manual sample were subjected to the 3D selection (which it is not because it is used to define it). So, for consistency reasons, the seven Cepheids are excluded. As described in the previous subsection, the seven Cepheids are flagged with the 64 bit flag. In the Appendix, the location of those seven Cepheids in the 3D space can be seen in Figures 32–34. The 3D classification finds an additional 3390 Cepheid candidates. As can be seen in Figure 8, 1922 of those are clipped due to the color cut.

3.6. Outlier Clipping

Figure 9 shows the Wesenheit PLR of the combined manual and 3D sample after all selection criteria have been applied. As

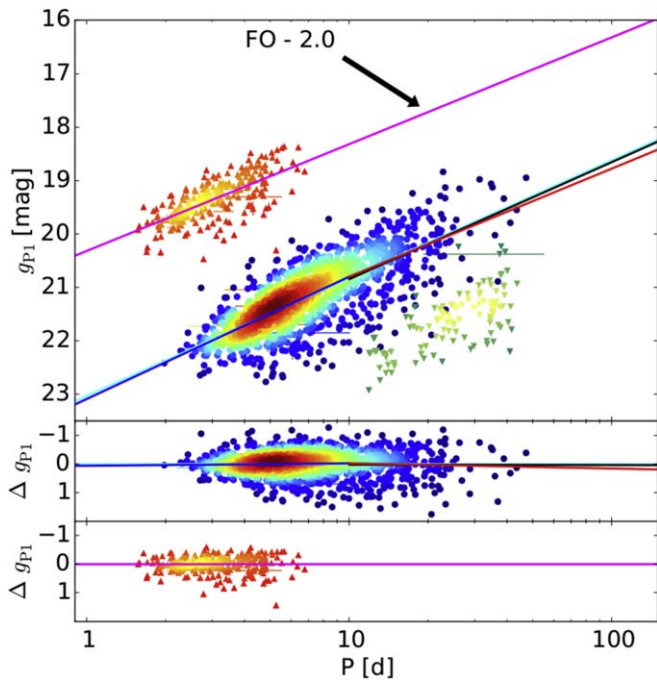


Figure 22. The g_{P1} -band PLR. The figure is analog to Figures 19 and 20 but shows fits #10, #11, and #12 from Table 3 and fit #4 from Table 4.

can be seen, there are outliers. There are different reasons for these outliers: crowding, misclassification, misidentification, blending, and extinction. In K15, we discussed those reasons in more detail, but we want to point out that the crowding problem is significantly more severe in these ground-based optical data than in the *HST* data. In order to remove the outliers from the sample, we perform an iterative κ - σ clipping with the median absolute deviation of the residuals as the magnitude error. This method that we developed in K15 is very robust and is also used in K18b, as well as in Riess et al. (2016) and Hoffmann et al. (2016). As in K15 and K18b, we use $\kappa = 4$. The clipped Wesenheit PLR shown in Figure 10 has no outliers anymore. In Figure 11, we show all Cepheids that were clipped, as well as the UN Cepheids. The UN Cepheids in this figure were assigned the UN type because the Cepheids are occupying a transitional region where the type classification is unsecure (see Section 3.3). In K13, the UN type was assigned only to the clipped Cepheids. Here the UN type is assigned to all Cepheids shown in Figure 11. After this point, we do not distinguish between the two reasons a Cepheid could have been assigned the UN type. The 3D parameter space of the final clipped sample is shown in Figures 12 and 13. In these figures, we already do not distinguish between the two UN type origins. The 3D parameter space is more densely sampled, and of course, it is similar to the manual sample shown in Figures 5 and 6, since the additional Cepheids have been selected by this 3D space. It can also be seen that in the final sample, the transitional region between Cepheid types is more prominently populated, and therefore there are more UN Cepheids in these regions than in the manual sample.

4. PAndromeda Cepheid Catalog

The PAndromeda Cepheid catalog consists of 1662 FM Cepheids, 307 FO Cepheids, 278 T2 Cepheids, and 439 UN Cepheids and is the largest and most homogeneous catalog of

Cepheids in M31. For all Cepheids, we provide the light curves, as well as the fitted parameters in electronic form. In the Appendix, we show an excerpt of the published tables and briefly discuss the fit parameters. We also provide the light curves and fit parameters of 2670 sources that have been cut for the various reasons discussed in the previous section. The Appendix also includes a comparison to the K13 data. As can be seen in Figure 14, many Cepheids in the r_{P1} band have a lot of epochs, and therefore the periods can be determined very accurately, as seen in Figure 15. An example light curve is shown in Figure 16. Typically, the K13 data have less epochs, as is also the case in the example light curve, and the phase zero point is arbitrary and therefore will be different. Note that because of the strict masking, some epochs present in K13 might be missing here. In some extreme cases, there are no epochs from a certain year of the observing campaign due to the masking. This is in part the reason that some Cepheids identified in K13 are missing in this sample. Some areas are completely masked, and those Cepheids can no longer be recovered. Here 140 Cepheids from K13 have no data due to masking, and 148 Cepheids do not make the initial cut, where we require the periods in the r_{P1} and i_{P1} bands to be similar to 1% and in a period range between 1.5 and 150 days. Those Cepheids are not included in the published light curves of the selected sources, because we do not publish the sources that do not make the first cut due to their large quantity. These 148 Cepheids are a rather large number of missing Cepheids, since all K13 Cepheids should make this simple cut. The strict masking can remove a significant number of epochs in one band such that the period cannot be determined precisely anymore. This is the reason, then, that the Cepheids do not make the first cut. Of the remaining 1721 Cepheids from K13, 1453 are part of the PAndromeda Cepheid catalog. The other 268 Cepheids are cut for various reasons. As with the other sources that have been cut, the light curves are also published, and the reason for the cut is encoded in the bit flag. A cross-identification table is provided with the published data. In the Appendix, we compare the Cepheid type of the two samples. The spatial distribution of FM and FO Cepheids shown in Figure 17 follows the ring structure in M31, while the T2 Cepheids shown in Figure 18 trace the M31 halo.

5. Results

The PLR fit parameters are summarized in Table 3, while the corresponding fits are shown in Figures 19–22. The T2 Cepheids are not the subject of this work, so they are shown without a fit. Fit parameters for long-period Cepheids ($\log(P) > 1$) are also provided. Due to the fact that the intrinsic dispersion of the PLR is much larger than the typical photometric error, we do not use the photometric errors shown in Figures 19–22 as a weight in the fit. Rather, we assign the same weight to each Cepheid. An alternative to this approach is the method used in Efstathiou (2014), namely, to quadratically add an internal dispersion factor σ_{int} to all photometric errors such that the χ^2 of the fit is 1. The resulting PLR fit parameters of this method are within the errors shown in Table 3. This is not surprising, since the resulting σ_{int} is much larger than the typical photometric error, and thus the weight is almost the same for each Cepheid. The error of each fit parameter is in the $\pm\sigma$ range around the fit parameter determined from a distribution of 10,000 bootstrapping samples. As mentioned previously, not all Cepheids have color-excess information

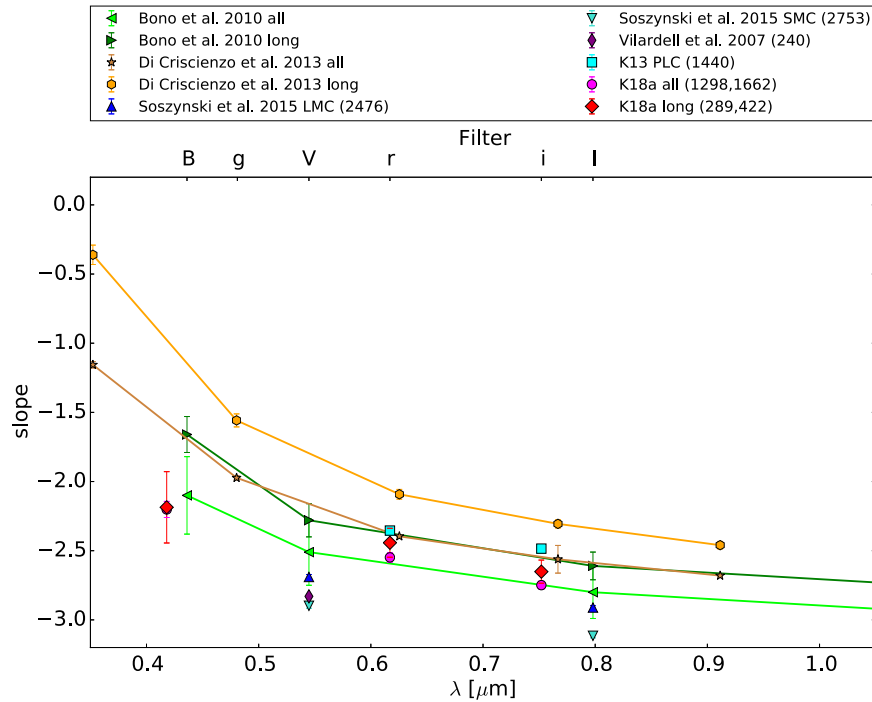


Figure 23. The PLR slope comparison with the literature for different wavelengths. Shown are the theoretical Bono et al. (2010) predictions from their Table 2 for $\log(Z/X) = -1.55$ and $0.4 \leq \log(P) \leq 2.0$ (all) and $\log(P) > 1.0$ (long). Also shown are the theoretical predictions from Di Criscienzo et al. (2013)’s Table 2 for $Z = 0.02$ and $\log(P) \leq 2.0$ (all) and $\log(P) \geq 1.0$ (long). Also shown are the LMC and SMC slopes from Soszyński et al. (2015)’s Table 2 for the V and I bands, as well as the slope obtained by Vilardell et al. (2007). The FM PLC slopes from K13’s Table 3 are also included (the slope errors in K13 have not been determined with the bootstrapping method). Also shown are the slopes of the complete sample (#4, #7, and #10) and of the sample of long-period Cepheids (#5, #8, and #11) from Table 3. Our slopes are steeper than in K13 but shallower than the LMC and SMC slopes. As in the theoretical predictions, our long-period Cepheid sample slopes are shallower than those for the complete sample.

Table 4
Broken-slope PLR Fit Parameters

| # | Band | N_{fit} | $b_{\log(P) \leq 1}$ | $b_{\log(P) > 1}$ | $a_{\log(P)=1}$ | σ |
|---|-----------|------------------|----------------------|-------------------|-----------------|----------|
| 1 | Wesenheit | 1662 | -3.461 (0.051) | -3.131 (0.050) | 19.715 (0.014) | 0.326 |
| 2 | r_{P1} | 1662 | -2.679 (0.054) | -2.368 (0.086) | 20.336 (0.017) | 0.353 |
| 3 | i_{P1} | 1662 | -2.883 (0.046) | -2.565 (0.068) | 20.176 (0.014) | 0.303 |
| 4 | g_{P1} | 1298 | -2.286 (0.077) | -2.021 (0.189) | 20.799 (0.025) | 0.433 |

Note. Two lines with a common suspension point at $\log(P) = 1$ are fitted. The magnitude errors were set to the same value. The errors of the fitted parameters were determined with the bootstrapping method.

from the Montalto et al. (2009) map, and therefore some Cepheid magnitudes are only corrected for foreground extinction. If we remove these from the PLR fit, the result stays the same within the given errors. Of course, some Cepheids might not be included in our sample because they are rejected in the color cut due to the missing color-excess information. The PLR dispersion is significantly reduced (by $\approx 25\%$) in the Wesenheit compared to K13. Also, the dispersion for the long-period sample is greatly reduced. The FM and FO PLR dispersion is also reduced or stays the same, as in the case of the r_{P1} -band PLR. Figure 23 shows a comparison of the slope values to other work. Compared to K13, our new slopes are shallower. The theoretical predictions of Bono et al. (2010) are quite close to our slopes. As in Bono et al. (2010) and Di Criscienzo et al. (2013), we also observe that the long-period sample slope is steeper than the slope of the complete sample. Due to the large scatter in the g_{P1} PLR, the slopes of the long-period sample and the complete

sample are almost identical. Our slopes are steeper than the slopes for the LMC and SMC in Soszyński et al. (2015).

In K15, we found a broken slope in the *HST* F110W and F160W data. The large dispersion in the ground-based data could make the identification of the broken slope more difficult. Table 4 shows the broken-slope fit with a common suspension point at $\log(P) = 1$. These fits are shown in Figures 19–22. As in K15, we test how significant the broken slope is by using the bootstrapping method. Figure 24 shows that the broken slope is not as significant as in K15, since the contour lines overlap. But it also shows that there are clearly two distinct distributions, except in the g_{P1} band. This is consistent with the significantly disjunct slopes shown in Table 4. In the g_{P1} band, the error of the slope for the long-period Cepheids is large, which is consistent with the fact that the long-period Cepheids in the g_{P1} band have a large scatter, and there are relatively few of them. So the fact that we do not observe the broken slope in the g_{P1} band might be due to the few epochs in the g_{P1} band, since a

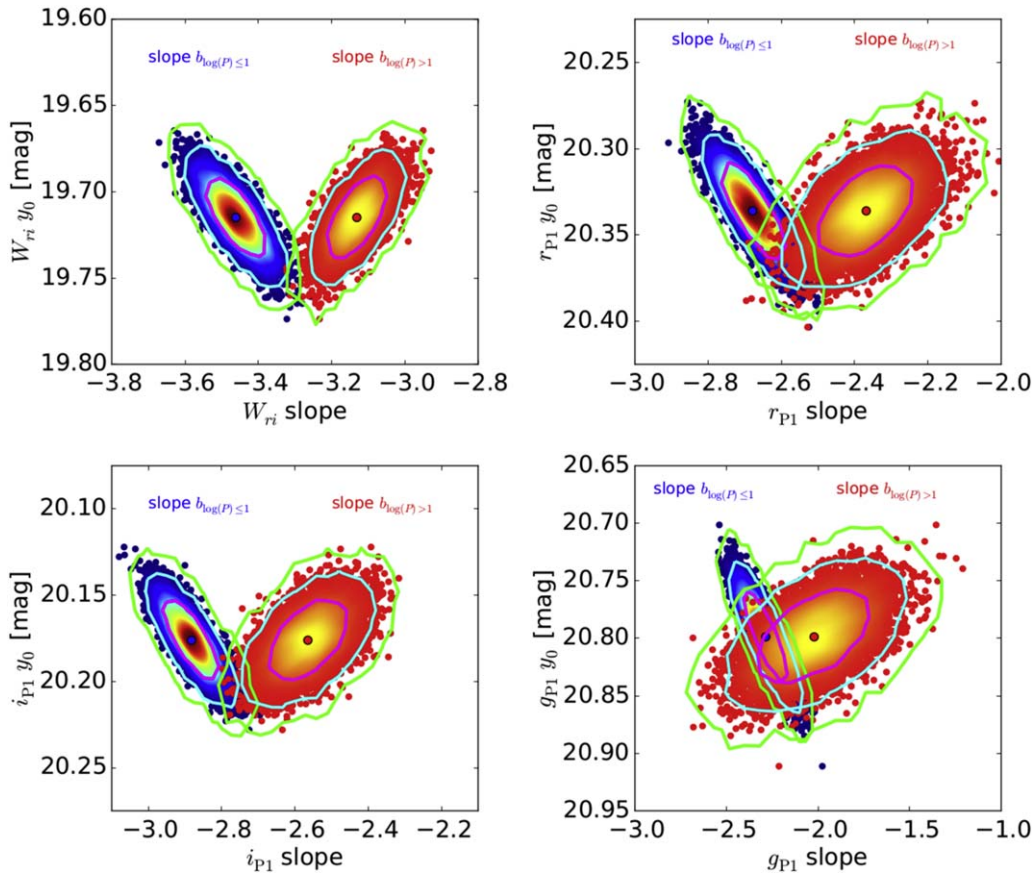


Figure 24. Bootstrapping of the broken-slope fit for the Wesenheit, r_{P1} , i_{P1} , and g_{P1} PLRs. Shown is the common suspension point y_0 vs. the slope. The points are colored according to the kernel density estimate. The 1σ , 2σ , and 3σ contour lines are shown as solid lines. The two distributions are clearly disjunct except in the g_{P1} band, which means that we find a broken slope, although the broken slope is not as significant as in that K15 because the contour lines overlap.

Table 5
Amplitude Ratio Fit Parameters

| # | Amplitude Ratio | Type | Range | N_{fit} | a ($\log P = 1$) | Slope b | σ |
|---|-------------------------|------|-------|------------------|----------------------|---------------|----------|
| 1 | $A_{r_{P1}}/A_{i_{P1}}$ | FM | All | 1662 | 1.224 (0.003) | 0.009 (0.012) | 0.137 |
| 2 | $A_{r_{P1}}/A_{g_{P1}}$ | FM | All | 1298 | 0.694 (0.005) | 0.059 (0.018) | 0.137 |
| 3 | $A_{r_{P1}}/A_{i_{P1}}$ | FO | All | 307 | 1.286 (0.032) | 0.113 (0.059) | 0.151 |
| 4 | $A_{r_{P1}}/A_{g_{P1}}$ | FO | All | 246 | 0.656 (0.032) | 0.005 (0.060) | 0.133 |

Note. The errors of the fitted parameters were determined with the bootstrapping method.

large error of the long-period slope can mask a possible broken slope in the g_{P1} band.

While the dispersion of the FO PLR decreased compared to K13, it is still not as nicely separated from the FM Cepheid PLR as in the *HST* data in K15 and K18b. This can best be seen in Figure 11, where some of the FO Cepheids overlay the FM Cepheids and vice versa (in Figure 19, we offset the FO Cepheids so that the two relations can be seen without the overlap). The FO-to-FM ratio is 0.18 and therefore twice the ratio in K13. This is closer to the ratio of 0.27 reported by Vilardell et al. (2007) for M31 and the ratio of 0.13 from the General Catalog of Variable Stars (Samus et al. 2017) for the Milky Way. As already described in K13, lower-metallicity objects like the SMC and LMC have higher FO-to-FM ratios on the order of 0.4–0.7 (Udalski et al. 1999). However, there

are significant uncertainties associated with our FO-to-FM ratio, mostly stemming from the type classification and the fact that we do not perform a completeness analysis. Especially, the lower-period cut is influencing our result.

We also determine amplitude ratios for our sample. Table 5 summarizes the fits shown in Figure 25. The amplitude ratio between the r_{P1} and i_{P1} bands decreases slightly compared to K13. As expected, the amplitude ratio between the r_{P1} and g_{P1} bands is smaller than 1, since the Cepheid amplitudes decrease with increasing wavelength (Madore & Freedman 1991). The obtained fits show no or only slight dependence on period. We also determine the phase lag between the three different bands. As can be seen in Figure 26, the phase lag is zero and independent of the period. This fact enabled us in K18b to correct the random phased *HST* data.

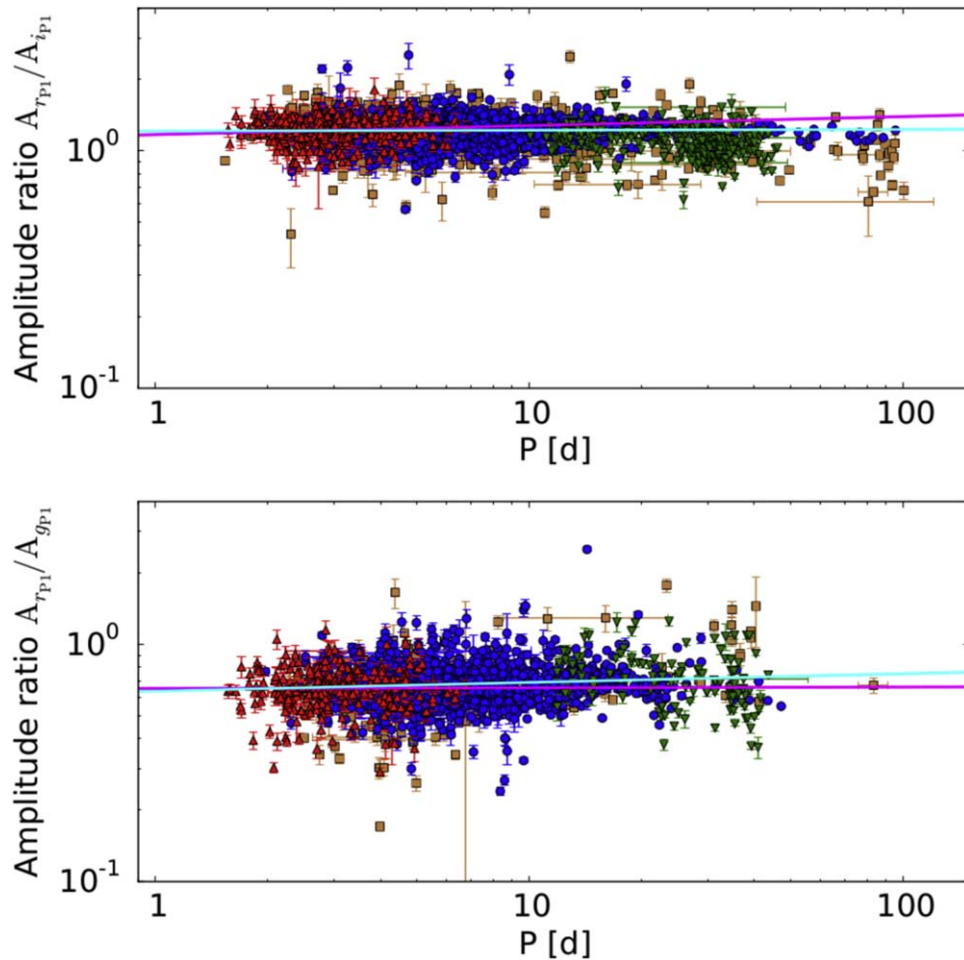


Figure 25. Amplitude ratio diagram. Shown are the two amplitude ratios $A_{r_{P1}}/A_{i_{P1}}$ (top panel) and $A_{r_{P1}}/A_{g_{P1}}$ (bottom panel). The fits from Table 5 are also shown (cyan line for FM Cepheids and magenta line for FO Cepheids). The amplitude ratios show no or only a slight dependence on period.

6. Conclusion

We use the PAndromeda data to obtain the largest and most homogeneous Cepheid sample in M31. We find 1662 FM Cepheids, 307 FO Cepheids, 278 T2 Cepheids, and 439 Cepheids with unclear Cepheid type. Similar to K13, we use a combination of a 3D Fourier parameter space, a color cut, and other selection criteria to find the Cepheids in as unbiased and reproducible a way as possible. We improved this approach by implementing a new type classification and using an improved color cut using the Anderson et al. (2016) instability strip edge models. The Anderson et al. (2016) instability strip edge models describe our data much better than the Fiorentino et al. (2002) instability strip edge models. However, the Anderson et al. (2016) instability strip does not cover a substantial fraction of the Cepheids that we classified manually (see Figure 2).

The PLRs we obtain in the r_{P1} , i_{P1} , and g_{P1} bands (see Figures 19–22) have smaller dispersions than in K13. This is achieved by a rigorous masking of the PS1 data and improved data reduction. As in K15, with *HST* data, we find a broken slope (see Figure 24), except in the g_{P1} band. The broken slope is not as significant as in K15.

We used the Cepheid sample obtained here in Kodric et al. (2018), where we obtained space-based *HST* PLRs in two near-infrared and two optical bands. The Kodric et al. (2018) Cepheid sample is the largest Cepheid sample in M31 with *HST* data. The PLR dispersions in the *HST* optical bands are similar to the dispersions obtained here with ground-based data. This means that the crowding effect on our ground-based but mean phase-corrected photometry is comparable to the effect of using random phased data in the *HST* sample. In K18b, we showed that the color selection can cause the

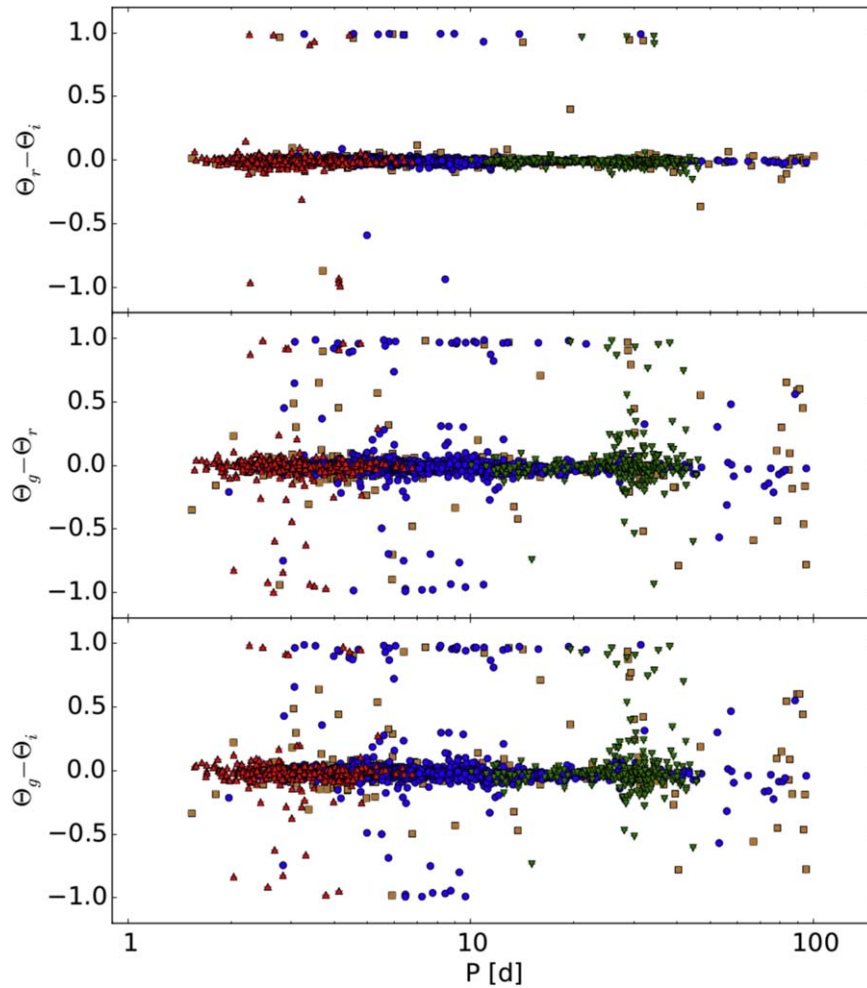


Figure 26. Phase lag between the r_{p1} and i_{p1} bands (top panel), g_{p1} and r_{p1} bands (middle panel), and g_{p1} and i_{p1} bands (bottom panel). The phase lag shows no dependence on period. The median phase lag is -0.007 , -0.011 , and -0.019 , respectively.

broken slope. Therefore, the new improved color cut could contribute to the observed broken slope.

The complete Cepheid catalog, including the light curves and objects clipped during the selection process, can be found electronically in the CDS database.

This research was supported by the DFG cluster of excellence Origin and Structure of the Universe (www.universe-cluster.de).

Appendix

A.1. Skycell Layout

The skycell layout discussed in Section 2.1 is shown in Figures 27–29 for K18a. Figures 30 and 31 show the skycell layout in K13.

A.2. Flag 64

The bit flag 64 is assigned seven times, as explained in Section 3.5. The seven manually classified Cepheids have a larger distance to their respective next Cepheid neighbor in 3D space. Figures 32 and 33 show the location of these seven Cepheids in the amplitude ratio (A_{21}) and phase difference

(φ_{21}) diagrams. Figure 34 shows where these seven Cepheids reside in the period Wesenheit diagram.

A.3. Comparison with K13

Since our data have more epochs and cover a larger time span than K13, the periods are also more precise. The long periods show a larger relative change in Figure 35, since for these periods, we now cover multiple pulsation cycles. We compare the r_{p1} - and i_{p1} -band magnitudes in Figures 36 and 37 for the 1445 Cepheids that are in both samples. There is no offset, but some Cepheids show a large magnitude change. The large magnitude differences are explained with a bad SExtractor position (on which the forced photometry was carried out) in K13 due to crowding. Most of these had a source position between two stars, and the brighter magnitude from this sample is now correct, since the position is correctly identified. But there are also a few cases where the new magnitude is fainter. This happens when there are two very close stars where the PSFs overlap and the pulsation was previously wrongly attributed to the brighter source. In Figure 38, we show how the Cepheid type changes. Of the 1445 Cepheids that are in both samples, 1224 do not change the Cepheid type. As can be seen, most change from UN to FM and from FM to UN, and almost all changes except for nine

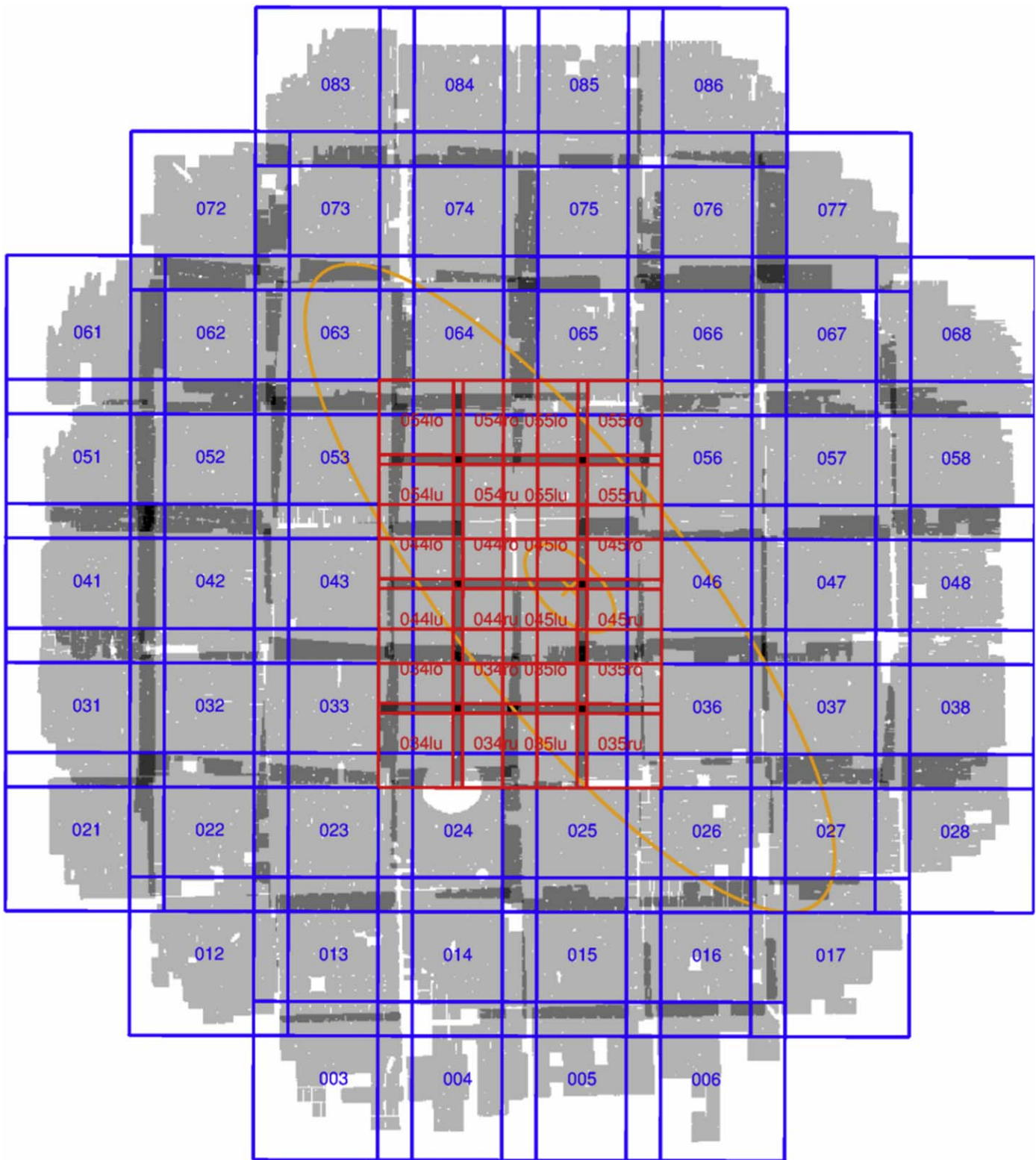


Figure 27. Skycell layout in the r_{p1} band. Each skycell covers $6647 \text{ pixels} \times 6647 \text{ pixels}$ (i.e., $27'.7 \times 27'.7$) and overlaps with the neighboring skycells. The six central skycells (red) are each divided into four smaller skycells with $3524 \text{ pixels} \times 3524 \text{ pixels}$ (i.e., $14'.7 \times 14'.7$) with an overlap between the skycells. The background in gray shows the unmasked area of the reference frames in the r_{p1} band. Darker shades of gray show the overlap between the skycells, with a maximum overlap of four skycells (black). The area covered is $\sim 7 \text{ deg}^2$. The orange cross marks the center of M31 and the orange ellipses are the $\mu_r = 20.05$ and 23.02 mag surface brightness profiles from Kent (1987).

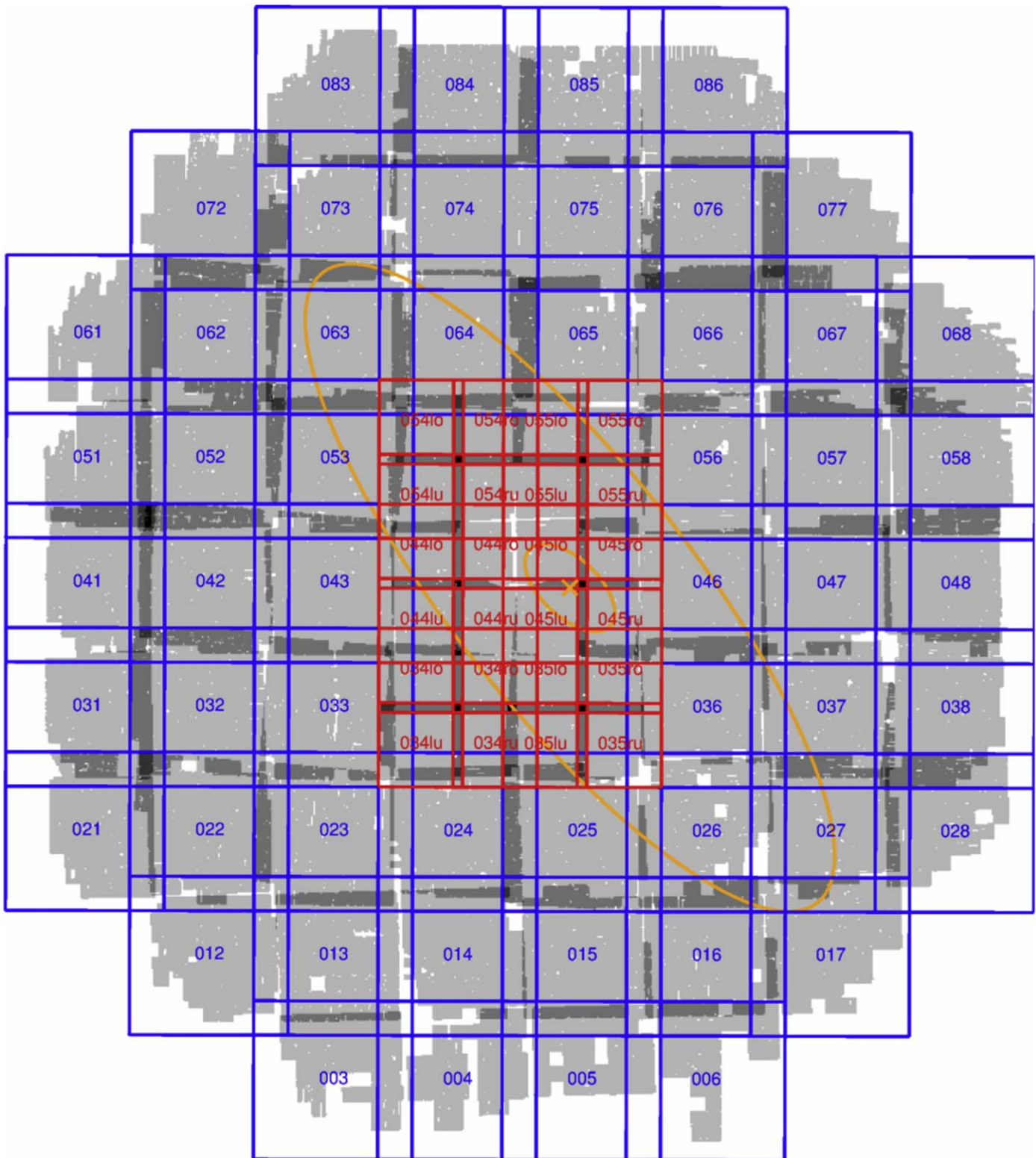


Figure 28. Skycell layout in the i_{p1} band. Same as Figure 27 but with the i_{p1} -band reference frames in the background. The area covered is $\sim 7 \text{ deg}^2$.

cases involve the UN type. A cross-match table is provided on the CDS.

A.4. Excerpt of the Published Tables

Tables 6–11 give a description of the published data. The tables include the clipped sources, but not all fits have

necessarily been performed for those objects, depending at which point the object was cut. In those cases, the columns show -1 or -99 as a default value. Some values can also be so small that they are shown as 0.0 in the tables. The errors of some values have been determined by different methods. We use the errors shown in Table 6. The method used to determine the magnitude errors is described in Section 3. A distribution of

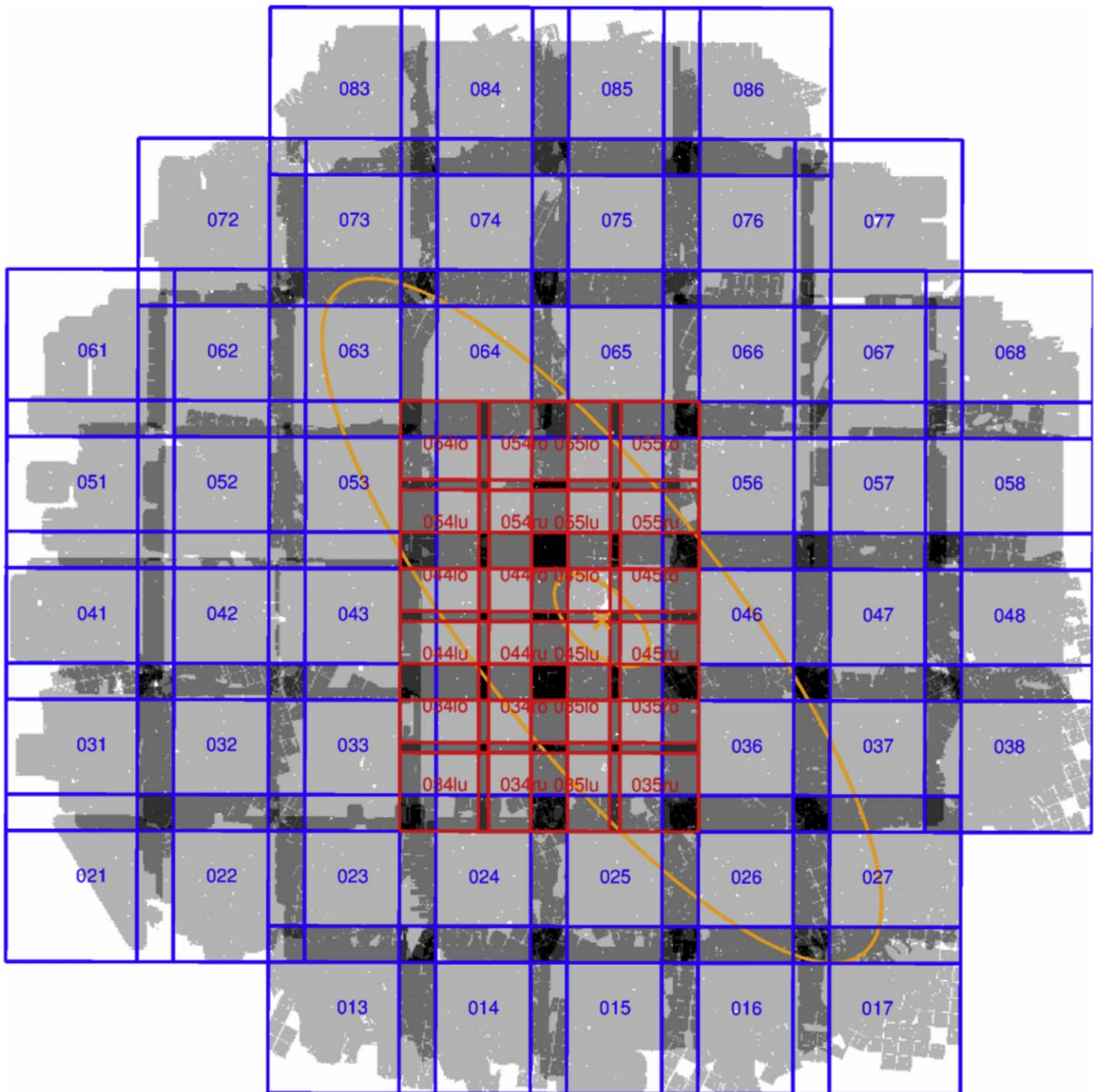


Figure 29. Skycell layout in the g_{p1} band. The g_{p1} reference frames are shown in the background, and skycells 003, 004, 005, 006, 012, and 028 are not used in the g_{p1} band, since there is almost no data. The area covered is $\sim 6.8 \text{ deg}^2$.

magnitudes is obtained, and the error is calculated from this distribution in two slightly different approaches. The first method is to determine the error from the $\pm\sigma/2$ range around the mean magnitude from the light-curve fit. The other method is to determine the error from the 1σ range of the distribution regardless of the fitted mean magnitude from the light curve. The two errors are the same if the mean of the distribution is the same as the mean magnitude from the light-curve fit. This also implies that the difference of these two error estimates is a tracer of how symmetric the distribution is around the mean magnitude from the light curve. A good example for this is the period error, where the distribution is obtained by using the

bootstrapping method on the light curve and the error is calculated with the two methods. The period calculated from the light curve can be so much on the edge of the distribution of periods obtained from the bootstrapping that it is outside the 1σ range of the distribution, and therefore the error from the $\pm\sigma/2$ range around the mean period is not defined anymore. The period of a light curve that is changed drastically when bootstrapping the light curve would show this behavior. Note that these Cepheids do not have poor period estimates but rather all epochs are important for the period determination. The error from the 1σ range can always be calculated, and therefore it is used as the period error. The $\pm\sigma/2$ range period

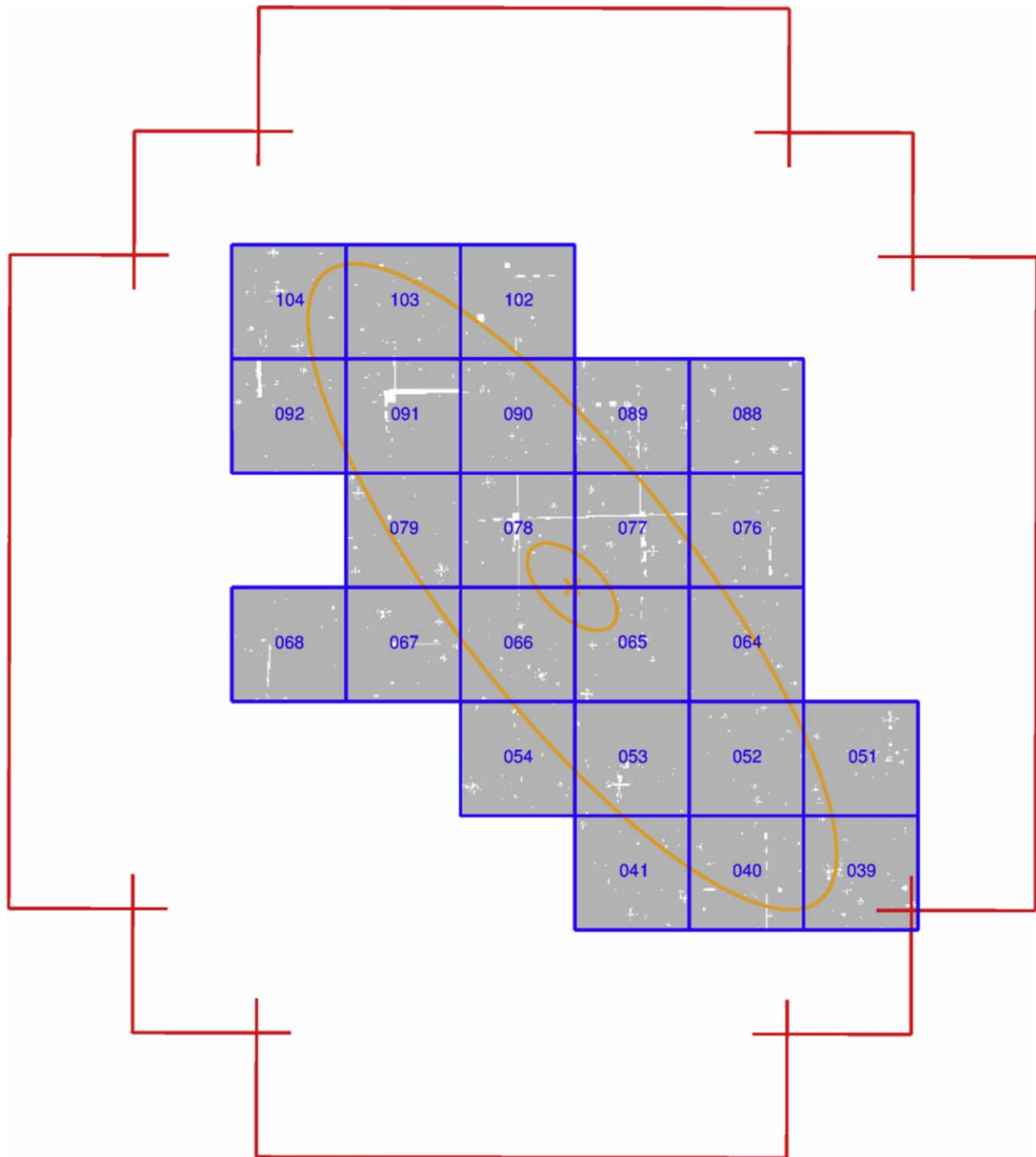


Figure 30. Skycell layout in the r_{p1} band in K13. In contrast to the data used here, the skycells have no overlap and cover $6000 \text{ pixels} \times 6000 \text{ pixels}$ (i.e., $20''.0 \times 20''.0$) in K13. The gray background shows the area covered in the r_{p1} -band reference frames in K13. The area covered is $\sim 2.6 \text{ deg}^2$. The orange cross marks the center of M31, and the orange ellipses are the $\mu_r = 20.05$ and 23.02 mag surface brightness profiles from Kent (1987). The red outline is the border of the skycells used in K18a (see Figure 27).

error would not be defined for all Cepheids. The different error estimates are not used in this work to perform additional cuts, but we include them in the published data for the interested reader.

In addition to the K13 cross-match table mentioned in the previous subsection, we also provide a cross-matching table for the Vilardell et al. (2006) sample with 416 Cepheids, the DIRECT sample with 332 Cepheids (Kaluzny et al. 1998,

1999; Stanek et al. 1998, 1999; Mochejska et al. 1999; Bonanos et al. 2003), the WECAPP sample with 126 Cepheids (Fliri et al. 2006), and the Riess et al. (2012) sample with 68 Cepheids. Due to the masking discussed in Section 2.1, we cannot match all literature Cepheids. With a matching radius of $2''$, we match 349 Cepheids of the Vilardell et al. (2006) sample of 416 Cepheids. Eight of the Vilardell et al. (2006) sample have two matches within the $2''$ radius. There are 277 Cepheids

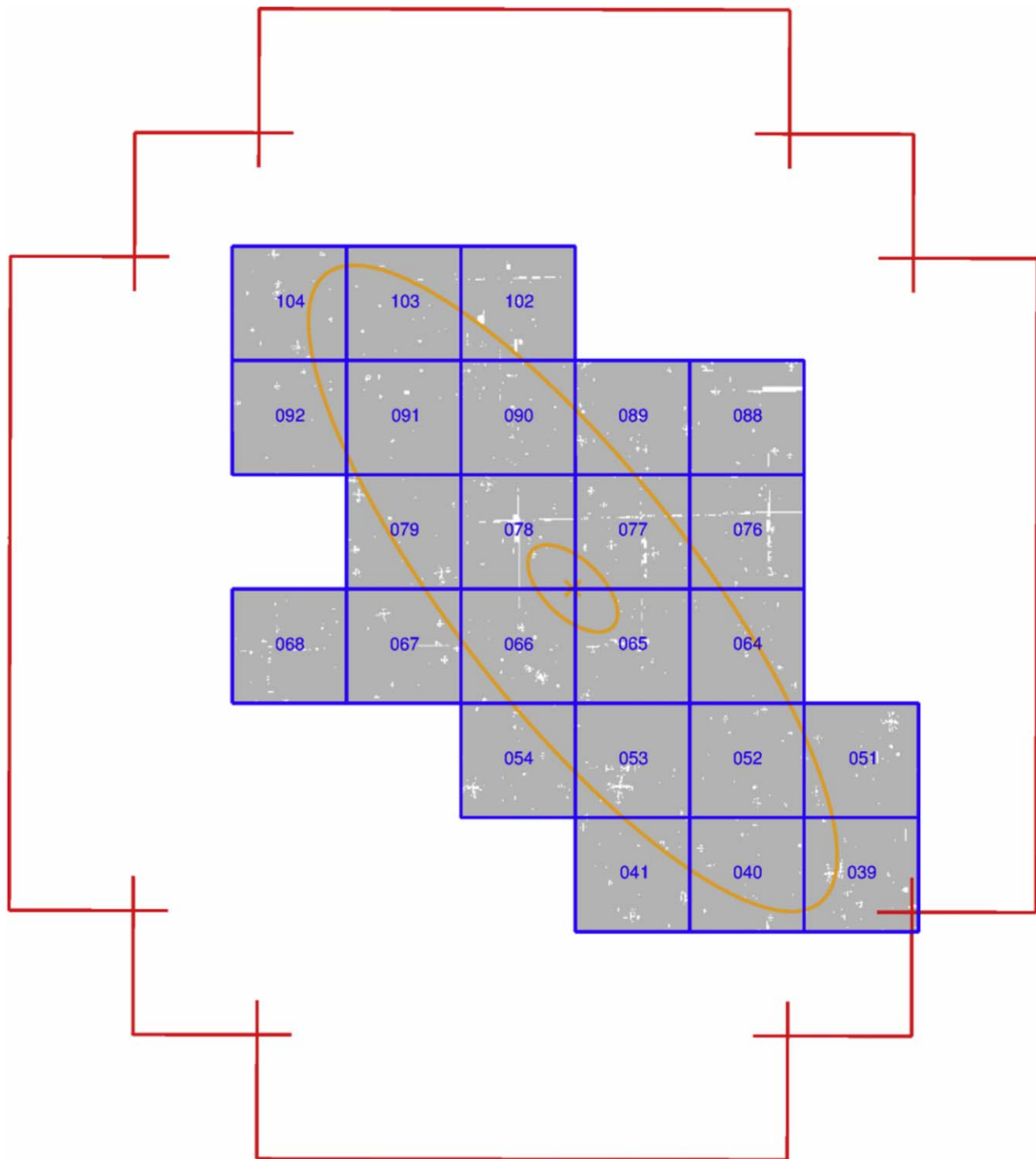


Figure 31. Skycell layout in the i_{p1} band in K13. The background shows the area covered in the i_{p1} -band reference frames in K13. Otherwise, the figure is the same as Figure 30. The area covered is $\sim 2.6 \text{ deg}^2$.

in the K18a sample, and 72 are clipped. Of the 332 DIRECT Cepheids, we match 316. There are 14 Cepheids with two matches inside the $2''$ matching radius, 267 are in the K18a sample, and 49 are clipped. Of the 126 WECAPP Cepheids, we match 64. Thirty are in the K18a sample while 34 are clipped, and two Cepheids have two matches inside the $2''$ matching radius. We match 61 of the 68 Riess et al. (2012) Cepheids. Three have two matches within the $2''$ radius, and 55 are in

K18a, while nine are clipped. In Figure 39, we show the comparison of the literature periods with those that are in our K18a sample (i.e., the clipped Cepheids are not included). The Vilardell et al. (2006) sample and the WECAPP sample have the most epochs of the literature samples, and therefore the periods match very well to our K18a periods. Since our K18a sample covers a larger baseline, the long periods are determined more precisely than in the literature samples.

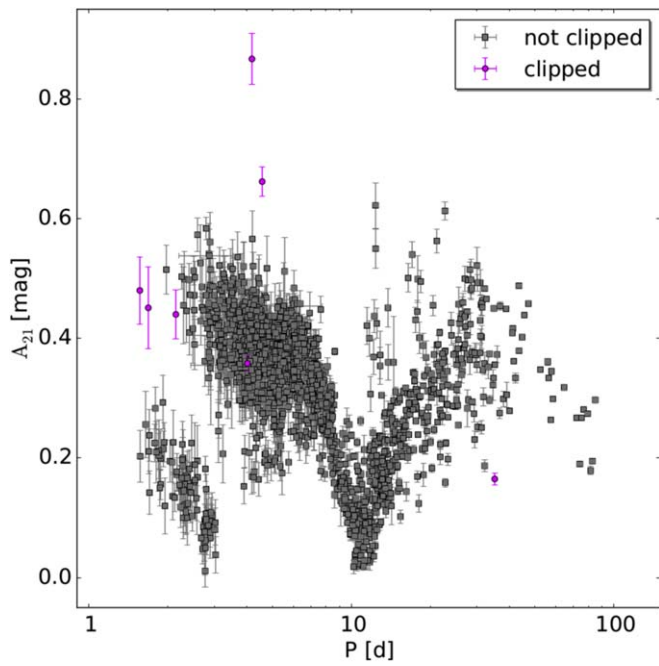


Figure 32. Amplitude ratio (A_{21}) diagram of the manually classified Cepheid sample. Shown are the 1640 Cepheids that are used for the final sample and the seven Cepheids that are assigned the bit flag 64. The reason that this bit flag is assigned is that those seven Cepheids have a large distance to their closest neighbor in 3D space.

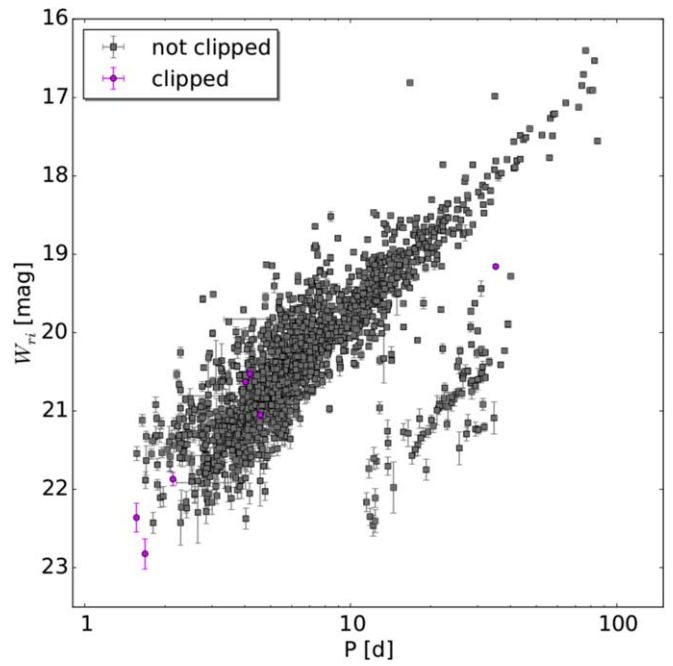


Figure 34. Period Wesenheit diagram. Shown are the seven Cepheids with the bit flag 64 and the 1640 Cepheids that are used for the final sample.

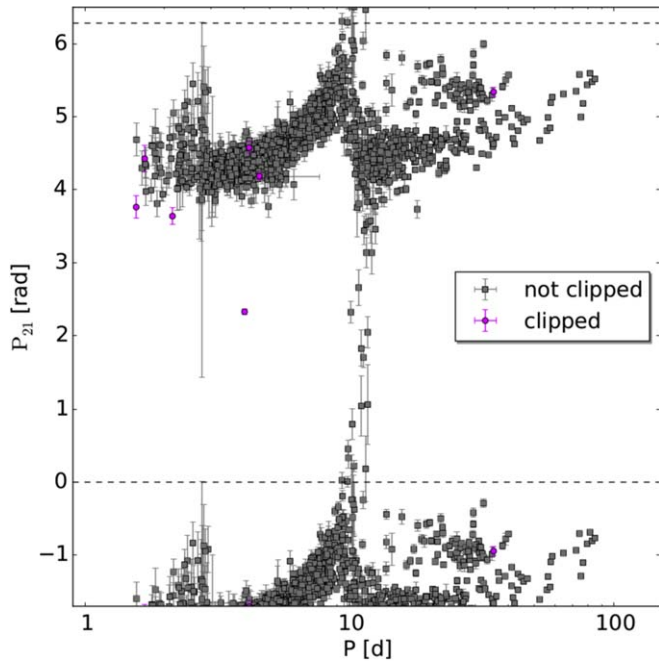


Figure 33. Phase difference (φ_{21}) diagram. Same as Figure 32 but the seven Cepheids with the bit flag 64 are shown with the 1640 manually classified Cepheids that are used in the final sample.

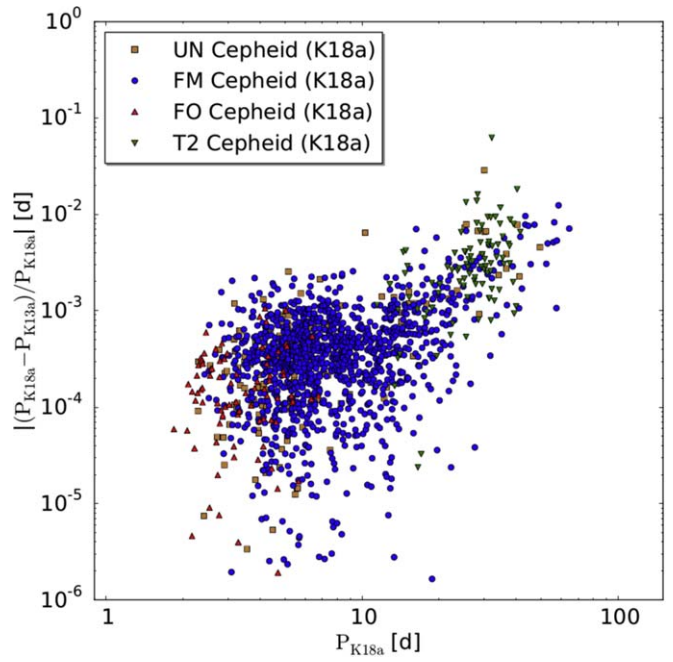


Figure 35. Comparison of the relative period change between this sample and K13. The long periods change by the largest amount, since we now cover multiple pulsations.

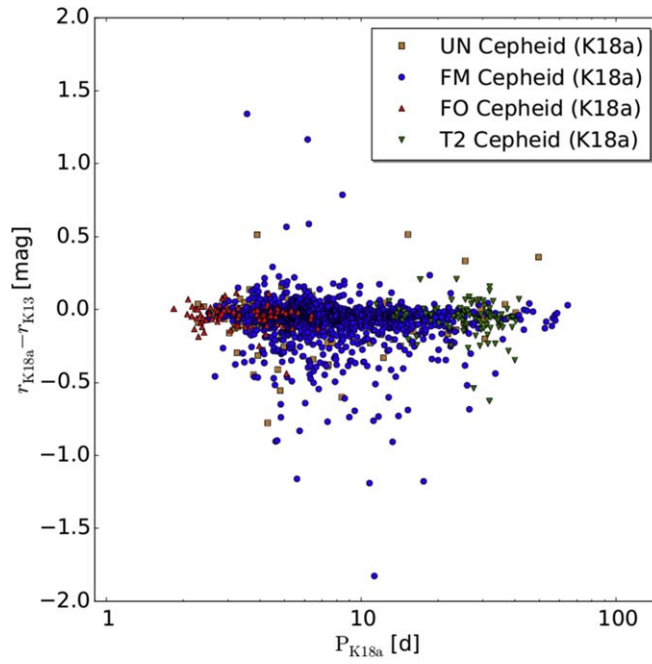


Figure 36. The r_{p1} -band comparison between this sample and K13 for the 1445 Cepheids that both samples have in common. The magnitudes here are not extinction-corrected. The large magnitude differences are explained with a bad SExtractor position (on which the forced photometry was carried out) in K13 due to crowding. Most of these had a source position between two stars, and the brighter magnitude from this sample is now correct, since the position is correctly identified. But there are also a few cases where the new magnitude is fainter. This happens when there are two very close stars where the PSFs overlap and the pulsation was previously wrongly attributed to the brighter source.

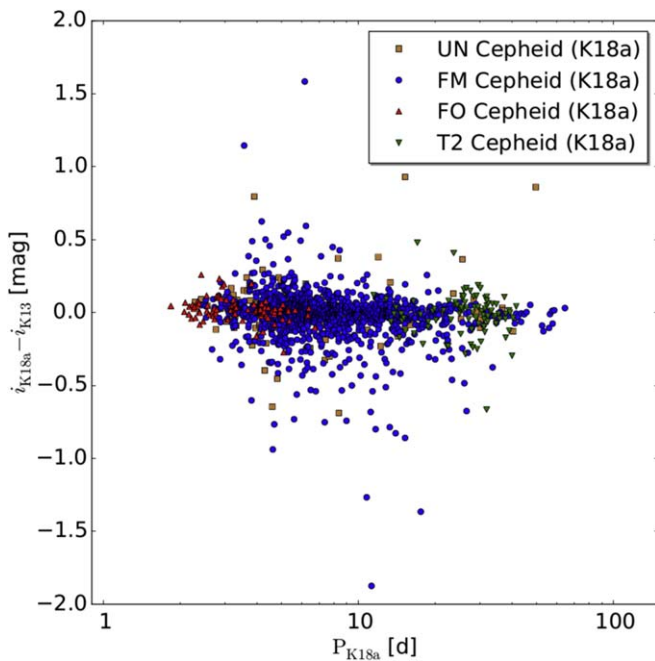


Figure 37. The i_{p1} -band comparison, otherwise the same as Figure 36.

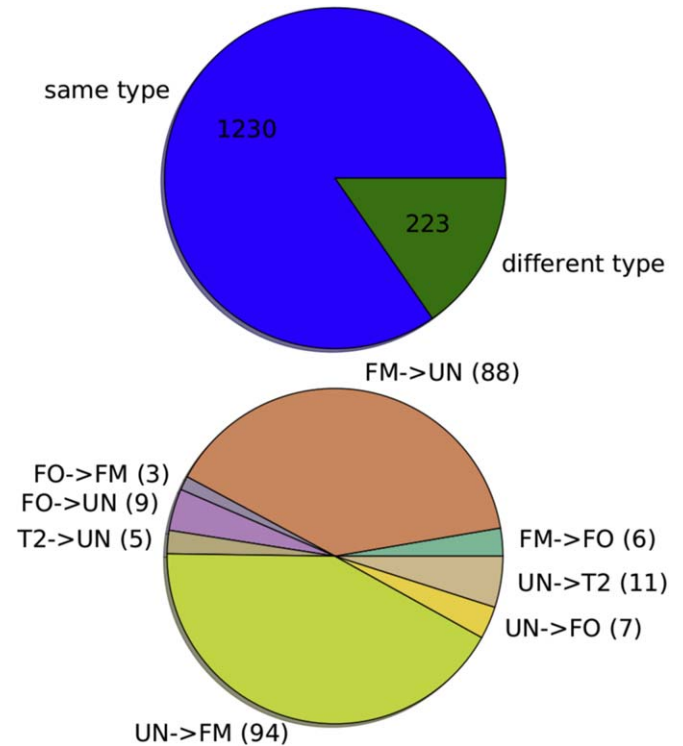


Figure 38. Cepheid type comparison for the 1445 Cepheids that are in this sample and K13. The Cepheid type changes for 221 Cepheids. Almost all of those changes except for nine cases involve the UN type.

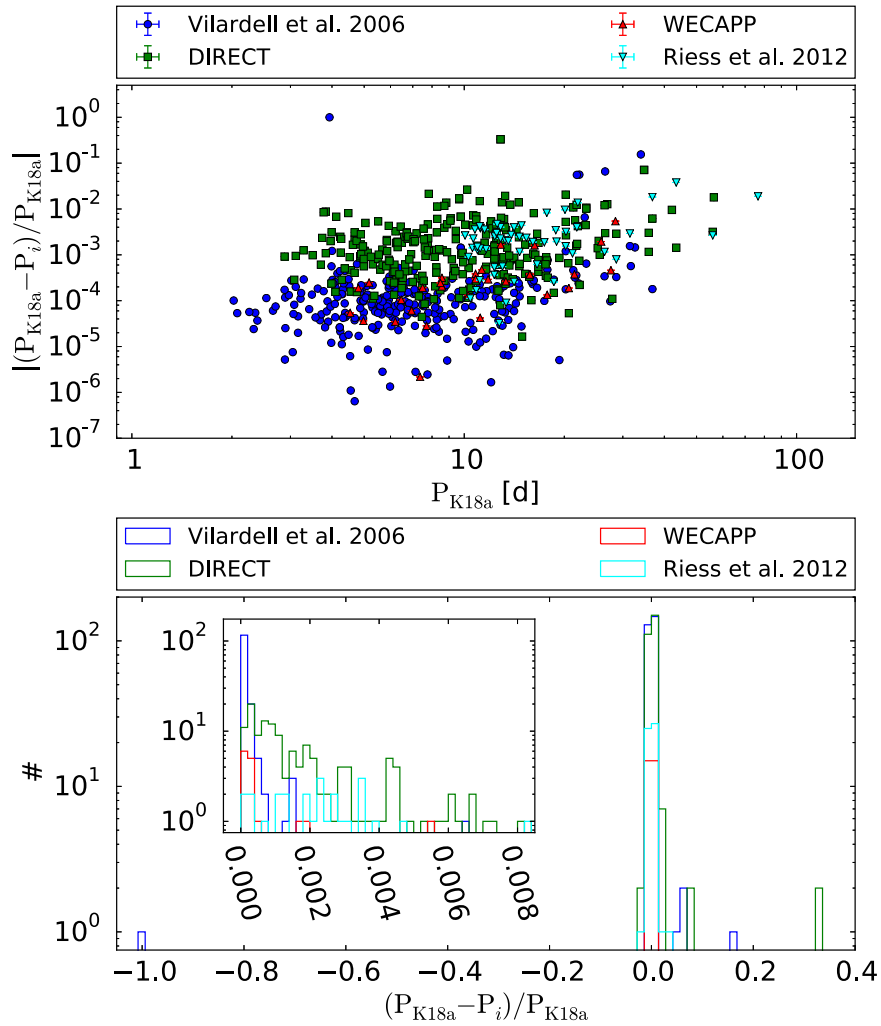


Figure 39. Comparison of the periods of our K18a sample with the literature samples. The top panel shows the absolute value of the relative period difference, while the bottom panel shows a histogram of the relative period difference. The Vilardell et al. (2006) sample and the WECAPP sample have a lot of epochs, and therefore the periods match very well to our K18a periods. The K18a baseline is longer than that for the literature samples, and therefore the period difference increases for larger periods.

Table 6
Description of main.dat

| Column # | Label | Explanation |
|----------|----------------|--|
| 1 | PSO id | PS1 identifier |
| 2 | id | Identifier used through the K18a data |
| 3 | R.A. | Right ascension (J2000.0) |
| 4 | Decl. | Declination (J2000.0) |
| 5 | $P_{r_{P1}}$ | Period in the r_{P1} band (determined with SigSpec) |
| 6 | $P_{e,r_{P1}}$ | Period error in the r_{P1} band determined with half the width of the 1σ interval of the period distribution obtained by the bootstrapping method |
| 7 | $r_{P1,0}$ | Extinction-corrected r_{P1} -band magnitude (mean flux of the light curve converted to magnitudes) |
| 8 | $r_{e,P1}$ | Magnitude error in the r_{P1} band determined by the method described in Section 3 |
| 9 | $i_{P1,0}$ | Extinction-corrected i_{P1} -band magnitude |
| 10 | $i_{e,P1}$ | Magnitude error in the i_{P1} band (see Section 3) |
| 11 | $g_{P1,0}$ | Extinction-corrected g_{P1} -band magnitude |
| 12 | $g_{e,P1}$ | Magnitude error in the g_{P1} band (see Section 3) |
| 13 | W | Wesenheit magnitude as defined in Equation (1) |
| 14 | W_e | Wesenheit magnitude error determined with the same method as $r_{e,P1}$; see Section 3 |

Table 6
(Continued)

| Column # | Label | Explanation |
|----------|-------------------------|--|
| 15 | A_{21} | Amplitude ratio of the first two Fourier components in the r_{P1} band (see K13 Equation (5)) |
| 16 | $A_{e,21}$ | Error of the amplitude ratio A_{21} obtained from the error of the Fourier decomposition |
| 17 | φ_{21} | Phase difference of the first two Fourier components in the r_{P1} band (see K13 Equation (6)) |
| 18 | $\varphi_{e,21}$ | Error of φ_{21} (same method used as for $A_{e,21}$) |
| 19 | sample | Manual in case the Cepheid was classified manually and 3D in case the Cepheid was classified with the 3D parameter space |
| 20 | flag $_{r_{P1},i_{P1}}$ | Bit flag for the r_{P1} and/or i_{P1} bands as described in Section 3.4 |
| 21 | flag $_{g_{P1}}$ | Bit flag for the g_{P1} band (see Section 3.4) |
| 22 | type | Cepheid type (see Section 3.3) |
| 23 | catalog | Flag indicating whether the object is part of the catalog (C) or has been clipped/rejected (R) |

(This table is available in its entirety in machine-readable form.)

Table 7
Description of lc-info.dat

| Column # | Label | Explanation |
|----------|----------------------------------|---|
| 1 | id | Identifier used through the K18a data |
| 2 | $\text{epo}_{r_{P1}}$ | Number of epochs in the r_{P1} -band light curve |
| 3 | $\text{epo}_{i_{P1}}$ | Number of epochs in the i_{P1} -band light curve |
| 4 | $\text{epo}_{g_{P1}}$ | Number of epochs in the g_{P1} -band light curve |
| 5 | $P_{i_{P1}}$ | Period in the i_{P1} band |
| 6 | $P_{g_{P1}}$ | Period in the g_{P1} band |
| 7 | $\text{sig}_{r_{P1}}$ | SigSpec significance of the r_{P1} -band period (see Section 3 in K13) |
| 8 | $\text{sig}_{i_{P1}}$ | Significance of the i_{P1} -band period |
| 9 | $\text{sig}_{g_{P1}}$ | Significance of the g_{P1} -band period |
| 10 | $\text{epo}_{\text{use},r_{P1}}$ | Number of epochs used for the Cepheid light curve in the r_{P1} band (all epochs are required to have a signal-to-noise ratio larger than two, and the corresponding visit stack has to have more than two frames) |
| 11 | $\text{epo}_{\text{use},i_{P1}}$ | Number of epochs used for the Cepheid light curve in the i_{P1} band |
| 12 | $\text{epo}_{\text{use},g_{P1}}$ | Number of epochs used for the Cepheid light curve in the g_{P1} band |
| 13 | min_r | Minimum magnitude (i.e., brightest magnitude) of the Fourier fit to the light curve in the r_{P1} band |
| 14 | min_i | Minimum magnitude of the Fourier fit to the light curve in the i_{P1} band |
| 15 | min_g | Minimum magnitude of the Fourier fit to the light curve in the g_{P1} band |
| 16 | max_r | Maximum magnitude (i.e., faintest magnitude) of the Fourier fit to the light curve in the r_{P1} band |
| 17 | max_i | Maximum magnitude of the Fourier fit to the light curve in the i_{P1} band |
| 18 | max_g | Maximum magnitude of the Fourier fit to the light curve in the g_{P1} band |
| 19 | r_{P1} | r_{P1} -band magnitude (i.e., not extinction-corrected as the $r_{P1,0}$ magnitude but also determined with the mean flux of the light curve converted to magnitudes) |
| 20 | i_{P1} | i_{P1} -band magnitude |
| 21 | g_{P1} | g_{P1} -band magnitude |
| 22 | $A_{21,i_{P1}}$ | Amplitude ratio in the i_{P1} band (analog to A_{21} but for the i_{P1} band) |
| 23 | $A_{21,g_{P1}}$ | Amplitude ratio in the g_{P1} band |
| 24 | $A_{e,21,i_{P1}}$ | Error of the amplitude ratio in the i_{P1} band (analog to $A_{e,21}$, i.e., error from the Fourier decomposition) |
| 25 | $A_{e,21,g_{P1}}$ | Error of the amplitude ratio in the g_{P1} band |
| 26 | $\varphi_{21,i_{P1}}$ | Phase difference of the first two Fourier coefficients in the i_{P1} band (analog to $\varphi_{21,g_{P1}}$) |
| 27 | $\varphi_{21,g_{P1}}$ | Phase difference in the g_{P1} -band |
| 28 | $\varphi_{e,21,i_{P1}}$ | Error of the phase difference in the i_{P1} band (analog to $\varphi_{e,21}$; the method described in Section 3 is used to determine the error) |
| 29 | $\varphi_{e,21,g_{P1}}$ | Error of the phase difference in the g_{P1} band |
| 30–40 | $a_{i,r_{P1}}$ | Fourier coefficients in the r_{P1} band as defined in Equation (3) in K13 (the order of the fit is $N = 5$, so there are 11 Fourier parameters) |
| 41–51 | $a_{i,i_{P1}}$ | Fourier coefficients in the i_{P1} band (the order of the fit is $N = 5$, therefore there are 11 Fourier parameters) |

Table 7
(Continued)

| Column # | Label | Explanation |
|----------|---------------|---|
| 52–62 | $a_{i,gP1}$ | Fourier coefficients in the g_{P1} band (the order of the fit is $N = 3$, but there are still 11 columns where the columns for the higher orders are set to a default value of -1) |
| 63–73 | $a_{i,e,rP1}$ | Fit error of the Fourier coefficients in the r_{P1} band |
| 74–84 | $a_{i,e,iP1}$ | Fit error of the Fourier coefficients in the i_{P1} band |
| 85–95 | $a_{i,e,gP1}$ | Fit error of the Fourier coefficients in the g_{P1} band |
| 96 | gap_{rP1} | Largest phase (Θ) gap in the folded r_{P1} -band light curve ($\Theta \in [0, 1]$) |
| 97 | gap_{iP1} | Largest phase gap in the folded i_{P1} -band light curve |
| 98 | gap_{gP1} | Largest phase gap in the folded g_{P1} -band light curve |
| 99 | catalog | Flag indicating whether the object is part of the catalog (C) or has been clipped/rejected (R) |

(This table is available in its entirety in machine-readable form.)

Table 8
Description of other.dat

| Column # | Label | Explanation |
|----------|----------------------|--|
| 1 | id | Identifier used through the K18a data |
| 2 | pretype | Cepheid type before the outlier clipping (see Section 3.6) |
| 3 | mult $_{rP1}$ | Number of different skycells in which the Cepheid is in the r_{P1} band |
| 4 | mult $_{iP1}$ | Number of different skycells in which the Cepheid is in the i_{P1} band |
| 5 | mult $_{gP1}$ | Number of different skycells in which the Cepheid is in the g_{P1} band |
| 6 | decrise $_{rP1}$ | Decline/rise factor in the r_{P1} band as defined in Section 5 in K13 |
| 7 | decrise $_{iP1}$ | Decline/rise factor in the i_{P1} band |
| 8 | decrise $_{gP1}$ | Decline/rise factor in the g_{P1} band |
| 9 | IV $_{rP1}$ | Noise factor in the r_{P1} band as defined by selection criterion IV in Table 1 |
| 10 | IV $_{iP1}$ | Noise factor in the i_{P1} band as defined by selection criterion IV in Table 1 |
| 11 | IV $_{gP1}$ | Noise factor in the g_{P1} band as defined by selection criterion IV in Table 2 |
| 12 | $E(B - V)$ | Color excess from the Montalto et al. (2009) map but improved where possible by the instability strip as discussed in Section 3.2 |
| 13 | err $_{rP1}$ | Magnitude error in the r_{P1} band determined from the 1σ range method |
| 14 | err $_{iP1}$ | Magnitude error in the i_{P1} band determined from the 1σ range method |
| 15 | err $_{gP1}$ | Magnitude error in the g_{P1} band determined from the 1σ range method |
| 16 | err $_{ok,rP1}$ | Percentage ($\in [0, 1]$) of r_{P1} -band epochs used in all 10,000 light-curve realizations (see Section 3; epochs can be cut if the sum of the drawn reference frame flux and difference frame flux is negative or the signal-to-noise ratio is smaller than two) |
| 17 | err $_{ok,iP1}$ | Percentage of i_{P1} -band epochs (analog to err $_{ok,rP1}$) |
| 18 | err $_{ok,gP1}$ | Percentage of g_{P1} -band epochs (analog to err $_{ok,rP1}$) |
| 19 | err $_{m,rP1}$ | Mean r_{P1} -band magnitude of the distribution used to calculate the error |
| 20 | err $_{m,iP1}$ | Mean i_{P1} -band magnitude of the distribution used to calculate the error |
| 21 | err $_{m,gP1}$ | Mean g_{P1} -band magnitude of the distribution used to calculate the error |
| 22 | err $_{sd,rP1}$ | Standard deviation of the r_{P1} -band distribution used to calculate the error |
| 23 | err $_{sd,iP1}$ | Standard deviation of the i_{P1} -band distribution used to calculate the error |
| 24 | err $_{sd,gP1}$ | Standard deviation of the g_{P1} -band distribution used to calculate the error |
| 25 | $A_{e,21,m,r}$ | Amplitude ratio error in the r_{P1} band determined from the 1σ range method |
| 26 | $A_{e,m,21,i}$ | Amplitude ratio error in the i_{P1} band determined from the 1σ range method |
| 27 | $A_{e,m,21,g}$ | Amplitude ratio error in the g_{P1} band determined from the 1σ range method |
| 28 | $A_{e,21,c,r}$ | Amplitude ratio error in the r_{P1} band determined from the $\pm\sigma/2$ range method |
| 29 | $A_{e,c,21,i}$ | Amplitude ratio error in the i_{P1} band determined from the $\pm\sigma/2$ range method |
| 30 | $A_{e,c,21,g}$ | Amplitude ratio error in the g_{P1} band determined from the $\pm\sigma/2$ range method |
| 31 | $\varphi_{e,m,21,r}$ | Phase difference error in the r_{P1} band determined from the 1σ range method |
| 32 | $\varphi_{e,m,21,i}$ | Phase difference error in the i_{P1} band determined from the 1σ range method |
| 33 | $\varphi_{e,m,21,g}$ | Phase difference error in the g_{P1} band determined from the 1σ range method |
| 34 | $\varphi_{e,c,21,r}$ | Phase difference error in the r_{P1} band determined from the $\pm\sigma/2$ range method |

Table 8
(Continued)

| Column # | Label | Explanation |
|----------|----------------------|---|
| 35 | $\varphi_{e,c,21,i}$ | Phase difference error in the i_{P1} band determined from the $\pm\sigma/2$ range method |
| 36 | $\varphi_{e,c,21,g}$ | Phase difference error in the g_{P1} band determined from the $\pm\sigma/2$ range method |
| 37 | $P_{e,iP1}$ | Period error in the i_{P1} band determined with the 1σ range method |
| 38 | $P_{e,gP1}$ | Period error in the g_{P1} band determined with the 1σ range method |
| 39 | $P_{e,c,rP1}$ | Period error in the r_{P1} band determined with the $\pm\sigma/2$ range method |
| 40 | $P_{e,c,iP1}$ | Period error in the i_{P1} band determined with the $\pm\sigma/2$ range method |
| 41 | $P_{e,c,gP1}$ | Period error in the g_{P1} band determined with the $\pm\sigma/2$ range method |
| 42 | $P_{e,ok,rP1}$ | Percentage ($\in[0, 1]$) of the 10,000 bootstrapped light curves in the r_{P1} band for which SigSpec was able to determine a period |
| 43 | $P_{e,ok,iP1}$ | Percentage ($\in[0, 1]$) of the 10,000 bootstrapped light curves in the i_{P1} band for which SigSpec was able to determine a period |
| 44 | $P_{e,ok,gP1}$ | Percentage ($\in[0, 1]$) of the 10,000 bootstrapped light curves in the g_{P1} band for which SigSpec was able to determine a period |
| 45 | $A_{e,21,m,b}$ | Amplitude ratio error in the r_{P1} band determined from the 1σ range method where the distribution is obtained from 10,000 bootstrapped light curves from the measured light curve (i.e., not the method described in Section 3, where the reference frame flux is drawn from a distribution) |
| 46 | $A_{e,21,c,b}$ | Amplitude ratio error in the r_{P1} band determined from the $\pm\sigma/2$ range method with bootstrapping |
| 47 | $\varphi_{e,21,m,b}$ | Phase difference error in the r_{P1} band determined from the 1σ range method with bootstrapping |
| 48 | $\varphi_{e,21,c,b}$ | Phase difference error in the r_{P1} band determined from the $\pm\sigma/2$ range method with bootstrapping |
| 49 | b_{FM} | Percentage ($\in[0, 1]$) of how often the FM type is assigned in the 10,000 realizations (i.e., criterion VI in Section 3.4; the Cepheid type is the pretype, i.e., the type before the outlier clipping) |
| 50 | b_{FO} | Percentage of how often the FO type is assigned |
| 51 | b_{T2} | Percentage of how often the T2 type is assigned |
| 52 | b_{UN} | Percentage of how often the UN type is assigned |
| 53 | $E(B - V)_{\min}$ | Smallest possible color excess determined from the Montalto et al. (2009) map and the instability strip edges, as described in Section 3.2 |
| 54 | $E(B - V)_{\max}$ | Largest possible color excess |
| 55 | catalog | Flag indicating whether the object is part of the catalog (C) or has been clipped/rejected (R) |

(This table is available in its entirety in machine-readable form.)

Table 10
Description of match-K13.dat

| Column # | Label | Explanation |
|----------|----------------|---|
| 1 | name | Identifier from the literature sample |
| 2 | id | Identifier used through the K18a data |
| 3 | sR.A. | Literature sample right ascension (J2000.0) |
| 4 | sDecl. | Literature sample declination (J2000.0) |
| 5 | R.A. | Literature sample right ascension (J2000.0) |
| 6 | Decl. | Literature sample declination (J2000.0) |
| 7 | sP | Literature sample period |
| 8 | P_{rP1} | Period in the r_{P1} band (determined with SigSpec) |
| 9 | sample | Literature sample identifier; DIR for the DIRECT sample (Stanek et al. 1998), R12 for the Riess et al. (2012) sample, V06 for the Vilardell et al. (2006) sample, and WEC for the WECAPP sample (Fliri et al. 2006) |
| 10 | catalog | Flag indicating whether the object is part of the catalog (C) or has been clipped/rejected (R) |
| 1 | name | Identifier from the K13 sample |
| 2 | id | id > 0: identifier used through the K18a data id = 0: rejected due to the first cut criterion (see Section 3) id = -1: masked area in K18a |
| 3 | flag | Flag indicating whether the object is part of the catalog (C) or has been clipped/rejected (R) |
| 4 | $r_{K13,P1,0}$ | K13 extinction-corrected r_{P1} -band magnitude |
| 5 | $i_{K13,P1,0}$ | K13 extinction-corrected i_{P1} -band magnitude |
| 6 | P_{rP1} | K13 period in the r_{P1} band (determined with SigSpec) |
| 7 | type | K13 Cepheid type |
| 8 | $r_{P1,0}$ | K18a extinction-corrected r_{P1} -band magnitude |
| 9 | $i_{P1,0}$ | K18a extinction-corrected i_{P1} -band magnitude |
| 10 | P_{rP1} | K18a period in the r_{P1} band (determined with SigSpec) |
| 11 | type | K18a Cepheid type (see Section 3.3) |

(This table is available in its entirety in machine-readable form.)

(This table is available in its entirety in machine-readable form.)

Table 11

Description of Light-curve Tables in the .tar.gz Package (FOLDER/cep_cut_FILTER_ID.dat)

| Column # | Label | Explanation |
|----------|--------------------|---|
| 1 | date | Modified Heliocentric Julian Date |
| 2 | mag | Magnitude |
| 3 | mag _{err} | Magnitude error |
| 4 | n_{exp} | Number of exposures contributing to the visit stack (see Section 2.2) |
| 5 | t | Total exposure time |
| 6 | sc | Skycell identifier (see Figures 27–29) |

Note. FILTER: r or i or g; FOLDER: can be lc_FILTER or lc_cut_FILTER; ID: K18a identifier. All of the light-curve tables are available in the .tar.gz package in the *Astronomical Journal*. The metadata header for each file is shown here for guidance regarding its form and content.

ORCID iDs

Stella Seitz  <https://orcid.org/0000-0003-3277-2243>
 Ralf Bender  <https://orcid.org/0000-0001-7179-0626>
 Christian Obermeier  <https://orcid.org/0000-0002-3819-8855>
 W. S. Burgett  <https://orcid.org/0000-0003-4401-9582>
 P. W. Draper  <https://orcid.org/0000-0002-7204-9802>
 K. W. Hodapp  <https://orcid.org/0000-0003-0786-2140>
 N. Kaiser  <https://orcid.org/0000-0001-6511-4306>
 N. Metcalfe  <https://orcid.org/0000-0001-9034-4402>
 J. L. Tonry  <https://orcid.org/0000-0003-2858-9657>
 R. J. Wainscoat  <https://orcid.org/0000-0002-1341-0952>

References

Abazajian, K. N., Adelman-McCarthy, J. K., Agüeros, M. A., et al. 2009, *ApJS*, **182**, 543
 Alard, C., & Lupton, R. H. 1998, *ApJ*, **503**, 325
 Anderson, R. I., Saio, H., Ekström, S., Georgy, C., & Meynet, G. 2016, *A&A*, **591**, A8
 Becker, M. R., Desmond, H., Rozo, E., Marshall, P., & Rykoff, E. S. 2015, arXiv:1507.07523
 Bertin, E., & Armouts, S. 1996, *A&AS*, **117**, 393
 Bonanos, A. Z., Stanek, K. Z., Sasselov, D. D., et al. 2003, *AJ*, **126**, 175
 Bono, G., Caputo, F., Marconi, M., & Musella, I. 2010, *ApJ*, **715**, 277
 Bressan, A., Marigo, P., Girardi, L., et al. 2012, *MNRAS*, **427**, 127
 Chambers, K. C., Magnier, E. A., Metcalfe, N., et al. 2016, arXiv:1612.05560
 Chen, Y., Bressan, A., Girardi, L., et al. 2015, *MNRAS*, **452**, 1068
 Chen, Y., Girardi, L., Bressan, A., et al. 2014, *MNRAS*, **444**, 2525
 Dalcanton, J. J., Williams, B. F., Lang, D., et al. 2012, *ApJS*, **200**, 18
 Di Criscienzo, M., Marconi, M., Musella, I., Cignoni, M., & Ripepi, V. 2013, *MNRAS*, **428**, 212
 Efsthathiou, G. 2014, *MNRAS*, **440**, 1138
 Fiorentino, G., Caputo, F., Marconi, M., & Musella, I. 2002, *ApJ*, **576**, 402
 Fliri, J., Riffeser, A., Seitz, S., & Bender, R. 2006, *A&A*, **445**, 423
 Freedman, W. L., & Madore, B. F. 2010, *ARA&A*, **48**, 673
 Freedman, W. L., & Madore, B. F. 2011, *ApJ*, **734**, 46
 Gaia Collaboration, Prusti, T., de Bruijne, J. H. J., et al. 2016, *A&A*, **595**, A1

García-Varela, A., Sabogal, B. E., & Ramírez-Tannus, M. C. 2013, *MNRAS*, **431**, 2278
 Gieren, W., Pilecki, B., Pietrzyński, G., et al. 2015, *ApJ*, **815**, 28
 Hodapp, K. W., Kaiser, N., Aussel, H., et al. 2004, *AN*, **325**, 636
 Hoffmann, S. L., & Macri, L. M. 2015, *AJ*, **149**, 183
 Hoffmann, S. L., Macri, L. M., Riess, A. G., et al. 2016, *ApJ*, **830**, 10
 Humphreys, E. M. L., Reid, M. J., Moran, J. M., Greenhill, L. J., & Argon, A. L. 2013, *ApJ*, **775**, 13
 Inno, L., Matsunaga, N., Bono, G., et al. 2013, *ApJ*, **764**, 84
 Kaiser, N., Aussel, H., Burke, B. E., et al. 2002, *Proc. SPIE*, **4836**, 154
 Kaluzny, J., Mochejska, B. J., Stanek, K. Z., et al. 1999, *AJ*, **118**, 346
 Kaluzny, J., Stanek, K. Z., Krockenberger, M., et al. 1998, *AJ*, **115**, 1016
 Kent, S. M. 1987, *AJ*, **94**, 306
 Kodric, M., Riffeser, A., Hopp, U., et al. 2013, *AJ*, **145**, 106
 Kodric, M., Riffeser, A., Seitz, S., et al. 2015, *ApJ*, **799**, 144
 Kodric, M., Riffeser, A., Seitz, S., et al. 2018, *ApJ*, in press, (arXiv:1807.08753)
 Koppenhoefer, J., Saglia, R. P., & Riffeser, A. 2013, *ExA*, **35**, 329
 Leavitt, H. S. 1908, *AnHar*, **60**, 87
 Leavitt, H. S., & Pickering, E. C. 1912, *HarCi*, **173**, 1
 Lee, C.-H. 2017, arXiv:1701.02507
 Lee, C.-H., Kodric, M., Seitz, S., et al. 2013, *ApJ*, **777**, 35
 Lee, C.-H., Koppenhoefer, J., Seitz, S., et al. 2014a, *ApJ*, **797**, 22
 Lee, C.-H., Riffeser, A., Koppenhoefer, J., et al. 2012, *AJ*, **143**, 89
 Lee, C.-H., Seitz, S., Kodric, M., et al. 2014b, *ApJ*, **785**, 11
 Madore, B. F. 1976, *MNRAS*, **177**, 215
 Madore, B. F. 1982, *ApJ*, **253**, 575
 Madore, B. F., & Freedman, W. L. 1991, *PASP*, **103**, 933
 Magnier, E. 2006, in *The Advanced Maui Optical and Space Surveillance Technologies Conf.*, ed. S. Ryan, 50
 Majaess, D., Turner, D., & Gieren, W. 2011, *ApJL*, **741**, L36
 Mochejska, B. J., Kaluzny, J., Stanek, K. Z., Krockenberger, M., & Sasselov, D. D. 1999, *AJ*, **118**, 2211
 Montalto, M., Seitz, S., Riffeser, A., et al. 2009, *A&A*, **507**, 283
 Ngeow, C., Kanbur, S. M., & Nanthakumar, A. 2008, *A&A*, **477**, 621
 Opolski, A. 1983, *IBVS*, **2425**, 1
 Pietrzyński, G., Graczyk, D., Gieren, W., et al. 2013, *Natur*, **495**, 76
 Reegen, P. 2007, *A&A*, **467**, 1353
 Riess, A. G., Casertano, S., Yuan, W., et al. 2018, arXiv:1804.10655
 Riess, A. G., Fliri, J., & Valls-Gabaud, D. 2012, *ApJ*, **745**, 156
 Riess, A. G., Macri, L. M., Hoffmann, S. L., et al. 2016, *ApJ*, **826**, 56
 Samus, N. N., Kazarovets, E. V., Durlevich, O. V., Kireeva, N. N., & Pastukhova, E. N. 2017, *ARep*, **61**, 80
 Sandage, A., Tammann, G. A., & Reindl, B. 2009, *A&A*, **493**, 471
 Schlafly, E. F., & Finkbeiner, D. P. 2011, *ApJ*, **737**, 103
 Schlegel, D. J., Finkbeiner, D. P., & Davis, M. 1998, *ApJ*, **500**, 525
 Soszyński, I., Udalski, A., Szymański, M. K., et al. 2015, *AcA*, **65**, 297
 Stanek, K. Z., Kaluzny, J., Krockenberger, M., et al. 1998, *AJ*, **115**, 1894
 Stanek, K. Z., Kaluzny, J., Krockenberger, M., et al. 1999, *AJ*, **117**, 2810
 Stetson, P. B. 1987, *PASP*, **99**, 191
 Tang, J., Bressan, A., Rosenfield, P., et al. 2014, *MNRAS*, **445**, 4287
 Tonry, J., & Onaka, P. 2009, in *Advanced Maui Optical and Space Surveillance Technologies Conf.*, ed. S. Ryan, 40
 Tonry, J. L., Stubbs, C. W., Lykke, K. R., et al. 2012, *ApJ*, **750**, 99
 Udalski, A., Soszyński, I., Szymański, M., et al. 1999, *AcA*, **49**, 223
 Udalski, A., Szymański, M. K., & Szymański, G. 2015, *AcA*, **65**, 1
 Valentijn, E. A., McFarland, J. P., Snigula, J., et al. 2007, in *ASP Conf. Ser.* **376**, *Astronomical Data Analysis Software and Systems XVI*, ed. R. A. Shaw, F. Hill, & D. J. Bell (San Francisco, CA: ASP), 491
 Vilardeell, F., Jordi, C., & Ribas, I. 2007, *A&A*, **473**, 847
 Vilardeell, F., Ribas, I., & Jordi, C. 2006, *A&A*, **459**, 32
 Vilardeell, F., Ribas, I., Jordi, C., Fitzpatrick, E. L., & Guinan, E. F. 2010, *A&A*, **509**, A70
 Wagner-Kaiser, R., Sarajedini, A., Dalcanton, J. J., Williams, B. F., & Dolphin, A. 2015, *MNRAS*, **451**, 724